Microporous and Mesoporous Materials 403 (2026) 114006

Contents lists available at ScienceDirect

Microporous and Mesoporous Materials

journal homepage: www.elsevier.com/locate/micromeso

Ce-impregnated acid functionalized mesoporous silica as catalyst for ethanol dehydration to ethylene

Oksana Dudarko [a,b,*], Veronika Tomina [a], Natalia Kobylinska [c,d], Dorota Duraczyńska [e], Katarzyna Pamin [e], Ewa Serwicka [e], Gulaim Seisenbaeva [b]

[a] Chuiko Institute of Surface Chemistry, National Academy of Science of Ukraine, 17 General Naumova Str., Kyiv, 03164, Ukraine
[b] Department of Molecular Sciences, Swedish University of Agricultural Sciences, Box 7015, SE-75007, Uppsala, Sweden
[c] A.V. Dumansky Institute of Colloid and Water Chemistry, National Academy of Science of Ukraine, Ak. Vernadskoho blvd. 42, Kyiv, 03142, Ukraine
[d] Nanomaterials and Nanotechnology Research Center (CINN-CSIC), Principality of Asturias, Av. de la Vega 4-6, El Entrego, 33940, Spain
[e] Jerzy Haber Institute of Catalysis and Surface Chemistry, Polish Academy of Sciences, Krakow, Poland

ARTICLE INFO

Keywords:
Heterogeneous catalysis
Acid functionalized silica
Solid acid catalysts
Ethanol conversion
Selective ethylene production

ABSTRACT

The catalytic performance of Ce-containing mesoporous silica, functionalized with phenylsulfonic and phenylsulfonic/phosphonic acid groups, was studied for the ethanol dehydration to ethylene reaction in the temperature range of 250 °C–500 °C. The SBA-15-type materials were prepared using a 'one-pot' hydrothermal method, and for comparison, the performance of a silica gel with grafted alkylsulfonic groups was also studied. The initial silica supports and Ce-containing catalysts were characterized by XRD, XPS, TEM, SEM/EDX, TGA, zeta potential measurements, etc. The characterization results showed that the morphology, structure, thermal and textural parameters of the catalysts remained largely unchanged following the impregnation of 0.1 M Ce^{3+} ions. The nature, amount, and availability of acid groups in the mesoporous framework were identified as key factors influencing the metal-impregnation process. According to DRIFT-IR spectroscopy, the functionalization with sulfonic groups binding Ce^{3+} ions led to the generation of Brønsted (B) and Lewis (L) acid sites, respectively. Importantly, the thermal stability analysis revealed that the number of strong B-sites rapidly diminished during desorption up to 500 °C, resulting in a notable decrease in the B/L ratio after treatment at high temperatures. At the same time, ethanol conversion and selectivity towards ethylene were found to augment with increased reaction temperature to 500 °C. The SBA/$PhSO_3H$/Ce catalyst demonstrated superior overall performance, characterized by high ethanol conversion (95 %) and the most favourable kinetic profile, including the lowest activation energy (48.2 kJ/mol) among all materials. In contrast, the Ce-containing SiO_2SO_3H/Ce catalyst exhibited the highest TON (5223.6 per hour), indicating superior intrinsic efficiency per active site. The reusability of the obtained catalysts in terms of stability and conversion was explained using a range of instrumental methods.

1. Introduction

The production of lower olefins, such as ethylene, from renewable resources has emerged as a major focus in sustainable chemistry [1]. As a fundamental raw material for the petrochemical industry, ethylene's global production exceeds 100 million tons annually [2]. The energy-intensive process of steam cracking is the current answer to this demand, and it relies on fossil fuel-based feedstocks such as naphtha. However, in response to growing geopolitical and economic volatility, as well as pressing environmental concerns, the search for greener alternatives has intensified [3]. The catalytic dehydration of bio-derived ethanol offers a particularly attractive and sustainable route to produce this essential building block for polymers [4]. This process provides a clear pathway toward reducing dependence on petroleum and minimizing the environmental impact of chemical manufacturing.

Bioethanol dehydration using solid acid catalysts is operated at temperatures ranging from 200 °C to 500 °C and proceeds as follows:

$$C_2H_5OH \xrightarrow{catalyst, T>200^\circ C} C_2H_4 + H_2O + 45kJ/mol \quad (1)$$

However, this process is often accompanied by the formation of

* Corresponding author. Chuiko Institute of Surface Chemistry, National Academy of Science of Ukraine, 17 General Naumova Str., Kyiv, 03164, Ukraine.
E-mail address: oksana.dudarko@slu.se (O. Dudarko).

https://doi.org/10.1016/j.micromeso.2025.114006
Received 18 June 2025; Received in revised form 16 December 2025; Accepted 18 December 2025
Available online 19 December 2025

undesirable by-products such as diethyl ether (DEE), acetaldehyde, CH_4, CH_3CH_3, propylene, CO_2, CO, H_2, etc. [5] At the same time the extent and strength of the solid acid sites on a catalysts are particularly important factors in controlling the catalytic dehydration reaction. Generally, the formation of ethylene and DEE is promoted in the presence of acid centers on the catalyst, while acetaldehyde is produced on redox centers. A key consideration is that this reaction is achieving the right balance between Brønsted and Lewis acid sites on the catalyst's surface. However, it has been demonstrated that an increased concentration of strong Brønsted acid sites enhances the production of ethylene, whereas weak Brønsted and Lewis acid sites predominantly promote the formation of diethyl ether [6,7]. It is also important to note that the reaction is thermodynamically controlled. While endothermic ethylene formation is favored at higher temperatures, exothermic diethyl ether formation is the dominant pathway at lower temperatures (Eqs (2)–(4)).

$$2C_2H_5OH \xrightarrow{catalyst, T<200\ ^\circ C} C_2H_5OC_2H_5 + H_2O - 25\ kJ\,/\,mol \quad (2)$$

$$C_2H_5OC_2H_5 \xrightarrow{catalyst, T>200\ ^\circ C} C_2H_4 + H_2O + 115\ kJ\,/\,mol \quad (3)$$

$$C_2H_5OH \xrightarrow{catalyst, T>200\ ^\circ C} C_2H_4O + H_2 + 184kJ\,/\,mol \quad (4)$$

The key challenge in this field is therefore to develop catalysts that can selectively promote the dehydration reaction to produce ethylene, while preventing the formation of by-products [8].

Among all the catalysts (homogenous and heterogenous), those based on *(a)* phosphoric acid systems [9,10], *(b)* heteropoly acid [11] (solid supported catalysts showed higher catalytic activity than the unsupported ones [12]), (c) metal oxides and mixed metal oxides (e.g. γ-Al_2O_3 [13], CeO_2 [14], aluminosilicates [15,16], WO_3/silicate [17], TiO_2/γ-Al_2O_3 [8], Co_3O_4/CeO_2 [18], La/CeO_2 [19], etc.), and *(d)* molecular sieves, especially zeolites (e.g., MFI-type (H-ZSM-5 [20]) and Rho-type [21]), are particularly important for the dehydration of alcohols. However, there were some limitations to the catalytic application of zeolite catalysts, e.g. selectivity for the target product [22]. Therefore, the stability of the material along with an efficient ethanol conversion to ethylene has been investigated through various surface modifications of zeolites by the incorporation of La [22,23], phosphorus [22,24], NaOH [25], Al_2O_3 [22], etc. Recently, Ouayloul and co-authors reported that a series of ZSM-5 catalysts with varying SiO_2/Al_2O_3 ratios (from 23 to 80) were synthesized and subsequently modified with Ce, P and La to optimize their acidic properties [26]. A key finding of this study was the substantial enhancement in ethylene selectivity achieved by treating the ZSM-5 catalysts with hetero elements. As a result, at 200 °C and atmospheric pressure, the ethylene selectivity of the catalyst with a SiO_2/Al_2O_3 molar ratio of 23:1 increased from approximately 0 %–53 % for the Ce-containing samples, with no change in ethanol conversion. The same trend was observed for the catalyst with a SiO_2/Al_2O_3 molar ratio of 80:1, which was attributed to an increase in Lewis acid sites after modification with Ce^{3+} ions. However, increasing the Ce content negatively impacted both ethanol conversion and ethylene selectivity. The high Ce content was leading to the formation of new agglomerated sites, which were inaccessible to the reactants and resulted in a lower yield per active site over time. Lastly, wet impregnation was found to be more advantageous over dry melt-infiltration for preparing the modified catalyst, because it favored water dissociation, which led to the formation of new Si-OH groups. These groups acted as weak acidic sites which, although they promote DEE formation, can also interact with Ce^{3+} ions, thereby optimizing the overall selectivity for C_2H_4 formation.

The catalytic activity of metallic nanoparticles [27], metal oxides [28], and metal complexes can be significantly increased by stabilizing them in a highly dispersed state on an solid support, such as nanostructured ordered silica (e.g., SBA-15, SBA-16, MCM-41, MCM-48) [29]. This strategy is critical for increasing the number of accessible active sites, thereby enhancing overall catalytic efficiency. For example, Aiube et al. [30] incorporated Ce^{3+} ions into MCM-41 materials to produce a catalyst for the solvent-free oxidation of benzyl alcohol to benzaldehyde, using various Ce(III) precursors ($CeCl_3$ and $Ce(NO_3)_3$), and demonstrated the formation of Ce–O–Si bonds during the condensation process, as well as the creation of CeO_2 nanoparticles during heating. In this context SBA-15 material is considered as a promising silica carrier for catalytic systems [29] including ethanol dehydration [31]. It has a well-developed specific surface, significant pore volume, thermal stability, and its unique porous structure can be used to stabilize fine particles of active components without leaching of metal ions. It was previously found that Rare Earth Elements functionalized SBA-15, in particular Ce-loaded SBA-15 materials exhibited high catalytic, and sorption applications of Ce-SBA-15 materials were of general interest [28,32,33]. Among the most widely studied modifications for ethanol dehydration was Al-SBA-15, where aluminum was incorporated into the silica framework. This substitution generated Brønsted acid sites, allowing efficient conversion of ethanol to ethylene [34,35]. The incorporation of transition metals such as Fe, Nb, or Cu further altered the catalyst characteristics, affecting acidity, stability, and coking resistance [36,37]. The reaction pathway was highly dependent on the operating temperature. At relatively low temperatures (200–250 °C), ethanol dehydration over acidic SBA catalysts predominantly yielded diethyl ether. As the temperature increased above 350 °C, the reaction shifted toward ethylene, a desired product for the biopolymer industry [38,39]. The advantages of SBA-based catalysts [40] were obvious: *(1)* their mesoporous structure facilitated molecular diffusion; *(2)* their surface could be designed to have a wide range of active sites, and *(3)* their thermal stability allowed for long-term operation. Compared to microporous zeolites, SBA-15 catalysts were less prone to pore blockage and coke deposition, making them promising candidates for industrial-scale bio ethylene production. The control of acidity and porosity makes SBA-based systems uniquely suited to balance the selectivity between ethylene and diethyl ether depending on the process requirements. However, the impact of pore structure changes and surface sulfonic groups on the catalytic activity of SBA-15 remained unclear [40,41], particularly in the context of ethanol dehydration to ethylene.

The aim of this work was to develop a new generation of Ce-containing organic-inorganic catalysts as a competitive alternative for existing catalyst for the dehydration of ethanol to ethylene. These catalysts were based on SBA-15-type ordered mesoporous silica, functionalized with phenyl (*-Ph*), phenylsulfonic (*-$PhSO_3H$*), phosphonic (*-$P(O)(OH)_2$*) groups and their combinations. For comparison, an amorphous silica gel with covalently grafted alkylsulfonic groups was also studied to evaluate the influence of the ordered framework of support on catalytic performance. The SBA-15- and silica gel-based mesoporous catalysts were prepared *via* one-step template method and post-synthesis grafting, respectively. The structural, textural, and thermal properties of these mesoporous materials were carefully controlled during the impregnation of Ce^{3+} ions, with a specific focus on achieving a high and uniform distribution of loaded metal ions. The remarkable catalytic performance, particularly regarding stability and conversion, was fully elucidated and mechanistically interpreted using a comprehensive suite of physicochemical characterization methods.

2. Experimental part

2.1. Chemicals

Sodium metasilicate ($Na_2SiO_3{\cdot}5H_2O$, Sigma, USA), silica gel 60 (Merck), phenyltriethoxysilane ($C_{12}H_{20}O_3Si$ (PhTES), 99 %, Gelest), trichlorvinylsilane ($C_2H_3Cl_3Si$, 97.0 %, Sigma-Aldrich), chlorosulfonic acid ($ClSO_3H$, 99 %, Sigma-Aldrich), diethylphosphatoethyltriethoxysilane ($C_{12}H_{29}O_6PSi$, DPTS, 98 %, Gelest), Pluronic® P123 (Poly (ethylene glycol)-block-poly(propylene glycol)-block-poly(ethylene glycol), 99 %, BASF Corporation, USA), sulfuric acid (H_2SO_4, 98.0 wt %, Sigma), Sodium bisulfite ($NaHSO_3$, ACS reagent, Sigma-Aldrich),

hydrochloric acid (HCl, 37.5 wt %, Sigma), ethanol (96.5 wt %, Alfa Aesar), sodium hydroxide (≥99 % NaOH, pellets for analysis EMSURE®, Merck) and potassium chloride (KCl, 99.997 %, Alfa Aesar) were used.

$CeCl_3 \bullet 7H_2O$ (99 %, CAS 18618-55-8, Ourchem) was applied for modifications of the silica samples. The $CeCl_3$ stock solution was prepared by dissolving the appropriate amounts of cerium chloride in deionized water without acid. The C_2H_5OH (ethyl alcohol absolute, 99.8 %, POCh) were used in the catalytic dehydration experiments.

All other chemicals were of analytical grade and used without further purification. Deionized water used in all experiments was obtained from the Milli-Q water purification system.

2.2. Preparation of the catalysts

2.2.1. Synthesis of SBA-15-type materials

The SBA-15-based materials were synthesized according to the procedure reported previously [42]. In brief, Pluronic® P123 (4 g) was dissolved in the mixture (40 mL H_2O + 32 mL HCl (37.5 %)). Separately, $Na_2SiO_3 \bullet 9H_2O$ (8 g) was dissolved in water (40 mL) at room temperature and added gradually to the template solution. Opalescence was observed in 1 min, and after 2 min the precipitate fell out over the entire volume. The mixture was stirred for 2 h at 40 °C. Then, solids are filtered. The obtained white precipitate is dried 1 h at 100 °C and calcined in a muffle furnace at 450 °C for 3 h.

The SBA-15-type functionalized mesoporous materials were prepared in a similar way to the bare matrix, but with the addition of the corresponding silanes (diethylphosphatoethyltriethoxysilane (*DPTS*) and phenyltriethoxysilane (*PhTES*)) to the template solution (Table 1). The reaction mixture was then treated hydrothermally in a Teflon tube at 80 °C for 20 h.

Importantly, for functionalized silica samples the template was removed by boiling in acidified ethanol (200 mL EtOH +1.5 mL HCl (37.5 %)) during 3 h (30 mL EtOH/HCl per 1 g of mesophase). The operation was repeated 4 times. Then, mesoporous samples were drying in vacuum at 110 °C. Sulfonation of phenyl groups of *SBA/Ph* and *SBA/Ph/PO$_3$H$_2$* samples with $ClSO_2OH$ in the presence of CH_2Cl_2 was applied for syntheses of *SBA/PhSO$_3$H* and *SBA/SO$_3$H/PO$_3$H$_2$* supports, respectively.

2.2.2. Synthesis of silica gel with grafted alkylsulfonic groups (SiO_2SO_3H)

Silica gel was refluxed in HNO_3 (65 %) for 5 h, washed with water, then dried and calcined for 8 h at 550 °C before further treatment. Then, it was heated with distilled trichlorovinylsilane (1 mmol/g SiO_2) in water-toluene mixture (50:50) at 100 °C for 12 h. Obtained material was washed several times with the toluene in the Soxhlet apparatus. The effectiveness of the silane removal was determined by qualitative reactions with $AgNO_3$. The sample was washed with distillate water to prepare for the next sulfonation reaction. The vinyl groups of the silica gel were sulfonated using a 10 % $NaHSO_3$ solution at 90 °C in an air-bubbling environment. The product was then washed with a solution of 10 % HCl and deionized water until neutral pH, followed by drying under vacuum at 120 °C [43]. For this sample, the conversion of vinyl groups to acidic sites was determined to be ~50 %.

Table 1
The ratio of reagents in the reaction mixture for synthesis of SBA-15 type catalysts.

Sample	Functional groups	Na_2SiO_3 (mmol)	PhTES (mmol)	DPTS (mmol)	Pluronic® P123 (g)
SBA	–OH	0.04	–	–	4
SBA/Ph	$-C_6H_5$	0.04	0.004	–	4
SBA/Ph/PO$_3$H$_2$	$-C_6H_5$/ $-PO_3H_2$	0.05	0.005	0.005	5

2.2.3. Impregnation of Ce^{3+} ions onto the mesoporous silica

The impregnation of Ce^{3+} was conducted in aqueous suspensions at room temperature for 4 h with 0.1 mol $L^{-1}$of $CeCl_3$ and 5g·L^{-1}concentration of the obtained materials. The samples were separated by filtration with paper filters (Whatman®, Grade 2), washed with distilled water until neutral pH, dried overnight at 60 °C in air, and dehydrated for 6 h at 110 °C under argon atmosphere. The Ce^{3+} ions concentration in the filtrate was determined by inductively coupled plasma optical emission spectrometry (ICP-OES) iCAP 6300 (Thermo Scientific, USA).

2.3. Characterization techniques

The structure of SBA-based materials was investigated by Powder X-ray diffraction (XRD) analysis. The small-angle ($2\theta = 0.5–4°$) XRD difractograms were acquired using a PANalytical X'Pert Pro diffractometer (Philips, Netherlands) operating with CuKα radiation ($\lambda = 1.54184$ Å). The XRD patterns were analyzed using the JCPDS data files.

The functional groups of the obtained materials were revealed by Fourier transform infrared spectroscopy (FTIR) using a Spectrum Two (PerkinElmer, USA) spectrometer in the 400–4000 cm^{-1} range with averaging 64 scans and a resolution of 1 cm^{-1}. The silica samples were previously grounded with solid KBr (reagent grade) at a ratio of 1:5.

N_2 adsorption/desorption measurements have been performed on a KELVIN 1042 (Costech International) gas sorption system at 77 K. Prior to the measurements, all samples have been degassed under high vacuum conditions in a Helium flow at 110 °C for 1 h.

The morphology and elemental distribution of the elements were characterized by scanning electron microscopy (SEM) using JEOL JSM-7500F equipped with the X-ray energy dispersive (EDX) system – INCA PentaFetx3. Two detectors were used and images were recorded in two modes; the secondary electron detector provided images of SEI and a backscattered electron detector provided BSE (COMPO) microphotographs. The samples were dried for 24 h and covered with chromium (20 nm) immediately before the measurements. Transmission electron microscopy (TEM) images of the samples were obtained using a JEM-1230 and JEM-2100F (JEOL, Japan) instruments.

Electrophoretic mobility measurements were conducted using a ZetaSizer Nano ZS analyzer (Malvern Instruments, UK) at room temperature with external electric field gradients of 6–15 V cm^{-1}. The ζ-potential values represent the average of three to five separate measurements with a reproducibility estimated at 2–3 %.

X-ray Photoelectron Spectroscopy (XPS) measurements were recorded using a Quantera II Scanning XPS Microscope (Physical Electronics). A low-energy flood-gun, with settings of 1.0 V and 20.0 μA, was used for charge compensation. For the survey spectra, a pass energy of 224 eV and a resolution of 0.8 eV were used. A pass energy of 55 eV and a resolution of 0.1 eV were employed for the high-resolution spectra. The sample powders were suspended in 99 % ethanol and deposited onto clean glass slides, with the solvent subsequently evaporated under a desktop lamp. The binding energy was calibrated against the C 1s peak at 284.8 eV from adventitious carbon. Data processing and analysis were performed using CASA XPS software and smoothed using a Savitzky-Golay algorithm (9 points).

The content of sulfonic functional groups was calculated based on the C (wt. %) and S (wt. %) data determined from the analysis of CHNS elements with Vario MACRO cube elementary analyzer (Elementar Analysensysteme GmbH, Germany).

The amount of available acidic groups in the silica-based supports was determined by pH-metric titration [43]. In brief, a batch of solid (0.1 g) was submerged in NaCl solution (0.1 mol•L^{-1}, 20 mL) for 12 h. Then, obtained suspension with a standard NaOH solution (0.1 mol•L^{-1}) was titrated with registration of pH values.

Thermogravimetric analysis (TGA) was performed using a DSC/TG thermal analyzer of Netzsch STA 409 PC LUXX (Netzch, Germany), in the temperature range 20–1000 °C, at a heating rate of 10 °C min^{-1} and

in the air flow (40 mL min^{-1}).

2.4. Optical measurements

Diffuse reflectance spectra were obtained using a Specord®250 Plus spectrophotometer (Analytik Jena, Germany), which was equipped with a diffuse reflectance accessory (integrated sphere). $BaSO_4$ pellet was used as the background standard ("*white body*").

The optical band gap (E_g) was calculated using the Tauc method [44], which relies on plotting the transformed absorbance data according to the equation:

$$[\alpha h\nu]^{1/n} = A(h\nu - E_g) \text{ or } [F(R_\infty)h\nu]^{1/n} = A(h\nu - E_g) \quad (5)$$

where α is the absorption coefficient, which, for diffuse reflectance measurements, is replaced by the Kubelka-Munk function ($F(R_\infty) = (1-R_\infty)^2/2R_\infty$); $R_\infty = R_{sample}/R_{standard}$ is the reflectance of an infinitely thick specimen; h is the Planck constant; ν is the photon's frequency; A is a proportionality constant, and the exponent $1/n$ is a coefficient dependent on the nature of the electronic transition (e.g., $n = 1/2$ for a direct allowed transition or n = 2 for an indirect allowed transition).

The E_g values were obtained from the Tauc plot by extrapolating the linear portion of the graph to the point, where the ordinate axis $[F(R)\,h\nu]^{1/n}$ equals zero.

2.5. Acidity measurements

The strength of acid sites on the catalysts was determined using DRIFT-IR spectrometer (Nexus 470 Nicolet, Thermo Scientific) to analyze the adsorbed pyridine (Py). For sample preparation, powdered materials were ground and pressed into thin self-supporting wafers which were then placed inside a vacuum-tight quartz cell for *in situ* analysis. Prior to Py adsorption, the samples were meticulously pre-activated under vacuum (10^{-6} mbar) at 150 °C, 250 °C, 350 °C and 450 °C for 3 h to ensure the complete removal of physically adsorbed water. Py vapor was subsequently introduced at an equilibrium pressure of 1.0 mbar for 5 min to saturate all active sites, after which the spectrum of the adsorbed Py was recorded. The spectra were recorded after each evacuation step with a resolution of 4 cm^{-1} and 64 scans accumulation, allowing for the quantification of sites remaining active at higher temperatures.

2.6. Catalytic tests

The decomposition of ethanol was carried out in a conventional flow type reactor under atmospheric pressure. Typically, a batch of catalyst (0.10 g) was mixed with 0.2 g of quartz and placed in a quartz reactor. The total flow rate of alcohol in the stream of the feed gas was 1.8 L·h^{-1}. Before the test, the catalyst was activated at 150 °C in an argon flow for 1 h. Catalysis tests were conducted within a temperature range from 250 °C to 500 °C. The initial concentration of C_2H_5OH was 99.8 wt%.

Detection conditions. The dehydration products were analyzed by gas chromatography with flame ionization detector (PerkinElmer 900) and Porapak S column. Helium was used as the carrier gas. Ethylene, diethyl ether and acetaldehyde were mainly detected in the gas phase under the test conditions.

The catalytic performance was reported in terms of average ethanol conversion ($K_{C_2H_5OH}$, %) and selectivity (S, %) using following equations (Eq (6) and (7)):

$$K_{C_2H_5OH} = \frac{(C_0 - C_e)}{C_0} \cdot 100\ \% \quad (6)$$

$$S = \frac{C_e}{(C_0 - C_e)} \cdot 100\ \% \quad (7)$$

where C_0 and C_e are the initial and equilibrium concentration of ethanol, respectively, while C_P is concentration of reaction product.

3. Results and discussion

3.1. Preparation and characterization of the catalysts

Two silica dioxide materials were tested as supports for catalysts: amorphous non-ordered mesoporous silica gel (*SiO_2*, Merck) and ordered mesoporous silica *SBA-15*-type. The sulfonic functional groups in silica supports were bound using two spacers (alkyl and phenyl). The presence of phenyl groups contributed to increased affinity of the environment of the active sites on the silica surface. For producing functionalized silica samples one-step synthesis during formation of ordered silica framework or post-synthesis grafting method *via* salinisation reaction. Phenylsulfonic (*SBA/PhSO₃H*) and phenylsulfonic/phosphonic (*SBA/PhSO₃H/PO₃H₂*) silica were prepared by sulfonation reaction of the *SBA/Ph* and *SBA/Ph/PO₃H₂* samples, respectively. For monofunctional surface layer with acidic groups, alkylsulfonic silica (*SiO₂/SO₃H*) was prepared by post-synthesis grafting from vinyl functional silica.

The synthesized materials possessed a well-developed mesoporous structure, with Type IV adsorption-desorption isotherms (Fig. S1) according to the IUPAC classification [45]. A characteristic feature of the materials was the steep rise in adsorbed volume at P/P_0 ~0.65, which reflected the capillary condensation of N_2 within their uniform mesoporous structure The specific surface areas of the samples were obtained in the range from 420 m^2/g to 672 m^2/g (Table 2), with the average pores in the meso-range (2.5–6.8 nm).

Zeta potential values were investigated across a wide pH range to provide an estimation of the acidic nature and surface charge behavior of the materials during alkalization (or acidification) (Fig. S2). A significant decrease in ζ potential to approximately −20 mV was observed for the sample with acidic groups (*SBA/PhSO₃H*) as the pH was increased from 2 to 11. This decrease contrasted with the behavior of the starting neutral material (*SBA/Ph*) and was attributed to the increased dissociation of various functional groups with different degrees of acidity. These groups included the native Si-OH groups and the incorporated phenyl and sulfonic groups. The progressive ionization of these groups in an aqueous medium led to a substantial negative charge on the surface, which was directly reflected in the increasingly negative zeta potential.

Examination of the solid acid properties of catalysts was crucial for understanding the dehydration process and for making improvements [41]. The most accurate information about nature and accessibility of the acid sites on the silica surface was obtained *via* acid-base titrations [41,43], which provided the potential of protons as a function of titrant concentration profiles (Fig. 1a). The low inflection in the titration curves was obtained for the weak acid sites of the pristine *SBA-15* and *SBA/Ph* samples. Simultaneously, an endpoint at *0.*45 mmol/g and *0.*80 mmol/g were detected for the *SiO₂/SO₃H* and *SBA/PhSO₃H* samples, respectively. This inflection of titration curve corresponded to the well-known high strength acidity of the sulfonic groups on the silica surface [43]. The titration curve of the *SBA/SO₃H/PO₃H₂* samples exhibited two endpoints, which divided the titration curve into three regions: neutralization of sulfonic acid groups, neutralization of phosphonic acid groups and then of the silanol groups.

The calculation of the quantity of functional groups of catalysts was conducted by means of the Gran method [46] (Fig. 1b). Generally, the amount of functional acidic groups of the studied silica increased up to *1.*45 mmol/g (Table 2). Catalyst *SBA/PhSO₃H/PO₃H₂* has the highest concentration of functional acidic groups of various nature. The concentration of functional groups, determined by elemental analysis was mostly in good agreement with titration results (Table 2). Furthermore, the content of sulfonic groups in the *SBA/PhSO₃H* and

Table 2
Textural parameters and amount of functional groups in the silica-based supports.

Sample	N_2 isotherms			XRD			Elemental analysis				Titration
	S_{BET},m^2/g	V_s, cm^3/g	d_m,nm	$d_{(100)}$, nm	a_0, nm	W, nm	C, %	H, %	S, %	C_L, mmol/g	C_L, mmol/g
SBA	672	0.93	6.8	16.1	19.1	12.3	0.4	0.9	–	–	–
SBA/Ph	663	0.67	5.6	15.4	17.8	12.2	14.5	1.6	–	1.63	–
SBA/PhSO$_3$H	551	0.65	5.6	13.5	15.6	10.0	12.2	1.4	5.4	1.69	0.80
SBA/SO$_3$H/PO$_3$H$_2$	420	0.56	4.7	13.4	15.7	14.0	7.9	0.5	3.1	0.96	0.63/1.45
SiO$_2$SO$_3$H	490	0.86	2.5	–	–	–	1.3	0.5	1.6	0.51	0.45

Notes. S_{BET} – specific surface area; *Vs* – sorption pore volume; d_m – average pore diameter; $d_{(100)}$ – d-spacing calculated from the (100) plane reflection, a_0 – unit cell parameter, *W* – wall thickness, C_L – concentration of functional groups.

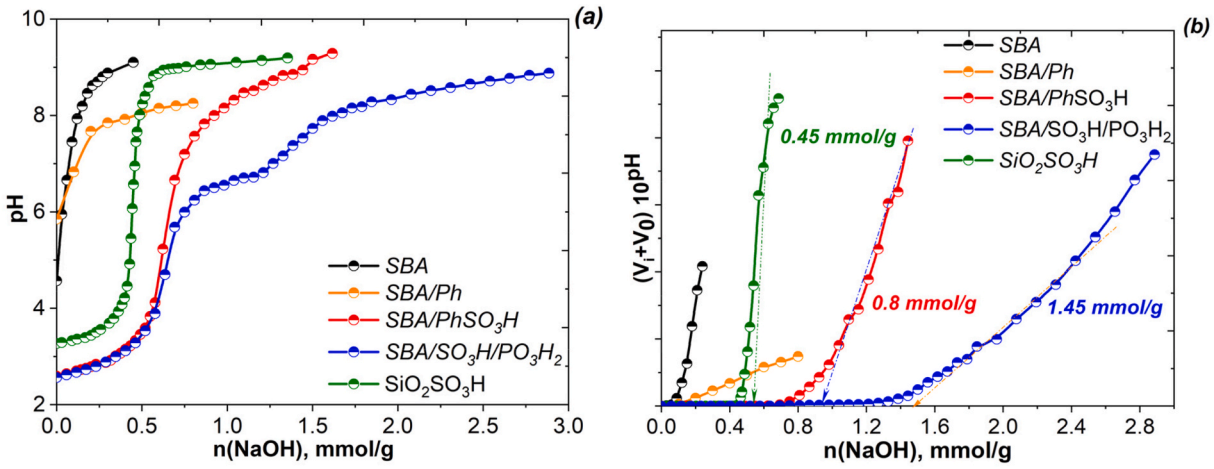

Fig. 1. Potentiometric titration curves *(a)* and their transformation according to Gran method *(b)* for the obtained materials.

SBA/SO$_3$H/PO$_3$H$_2$ materials, as calculated from elemental analysis, exceeded the values determined by titration by a factor of 2.7 and 1.5, respectively. This finding indicated their limited availability for external interactions, which could be attributed to their physical location inside the porous structure or other forms of steric inhibition.

Electrokinetic analysis was performed to evaluate the change in the surface charge of obtained mesoporous materials upon interaction with Ce^{3+} ions. The ζ-potential measurements were conducted *via* electrophoresis on dilute aqueous dispersions of mesoporous silica, as presented in Fig. 2.

As shown in Fig. 2, the presence of Ce^{3+} ions significantly altered the electrokinetic properties of the silica surface. At low concentrations,

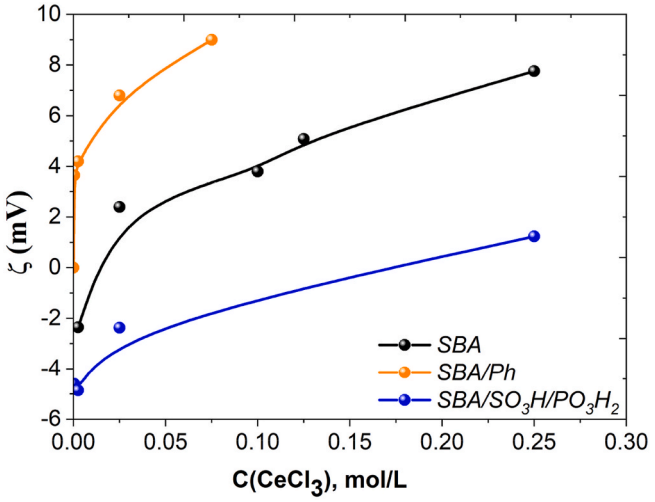

Fig. 2. The effect of $CeCl_3$ on the electrokinetic potential of the silica.

these ions adsorbed to the negatively charged surface, effectively neutralizing a portion of the surface charge and causing the ζ-potential to become less negative. As the concentration of Ce^{3+} ions increase, the continued adsorption leads to a charge reversal, changing the ζ-potential from negative to positive. This phenomenon can induce particle aggregation due to the reduction of electrostatic repulsion between the silica particles. In order to minimise this effect, the concentration of Ce^{3+} ions were limited to *0.*10 mmol/L during the preparation of the catalysts.

Based on the SEM data (Fig. 3), no significant changes in the morphology of the catalysts were observed after the impregnation of Ce^{3+} ions. The *SiO$_2$SO$_3$H/Ce* sample displayed the typical morphology of xerogel-like silica, consisting of spherical particles aggregated into a bulk structure (Fig. 3a). The *SBA/Ce* sample morphology was characteristic of SBA-15 type materials [47], with elongated particles forming a noodle-like structure (Fig. 3b). Similarly, the *SBA/Ph/Ce* and *SBA/PhSO$_3$H/Ce* samples showed a heterogeneous morphology, composed of irregularly shaped aggregates of rod-like and spherical sub-particles (Fig. 3c and d). In contrast, the *SBA/SO$_3$H/PO$_3$H$_2$/Ce* sample, a mesoporous SBA-15 type material with both phosphonic and phenylsulfonic groups, was composed of primary spherical particles arranged into globular aggregates (Fig. 3e). This sample was noticeably finer than the others. These morphological characteristics, particularly the finer particle size, could potentially increase the availability of active sites for catalytic reactions. Thus, the morphologies of the silica-based matrices were highly dependent on the synthesis methods and the specific silane components used during their preparation [48].

In order to confirm the preservation of the SBA-15 mesoporous structure throughout the impregnation process, the XRD analysis was performed (Fig. 4). A key observation from XRD patterns was the presence of the reflection peaks at 2θ between 0.7° and 1.5°. These peaks, which were indexed as the (100), (110), and (200) planar symmetries of the *P6mm* space group, confirmed the highly ordered 2D hexagonal structure characteristic of SBA-15 [42]. Also, the d-spacing (d_{100}) and

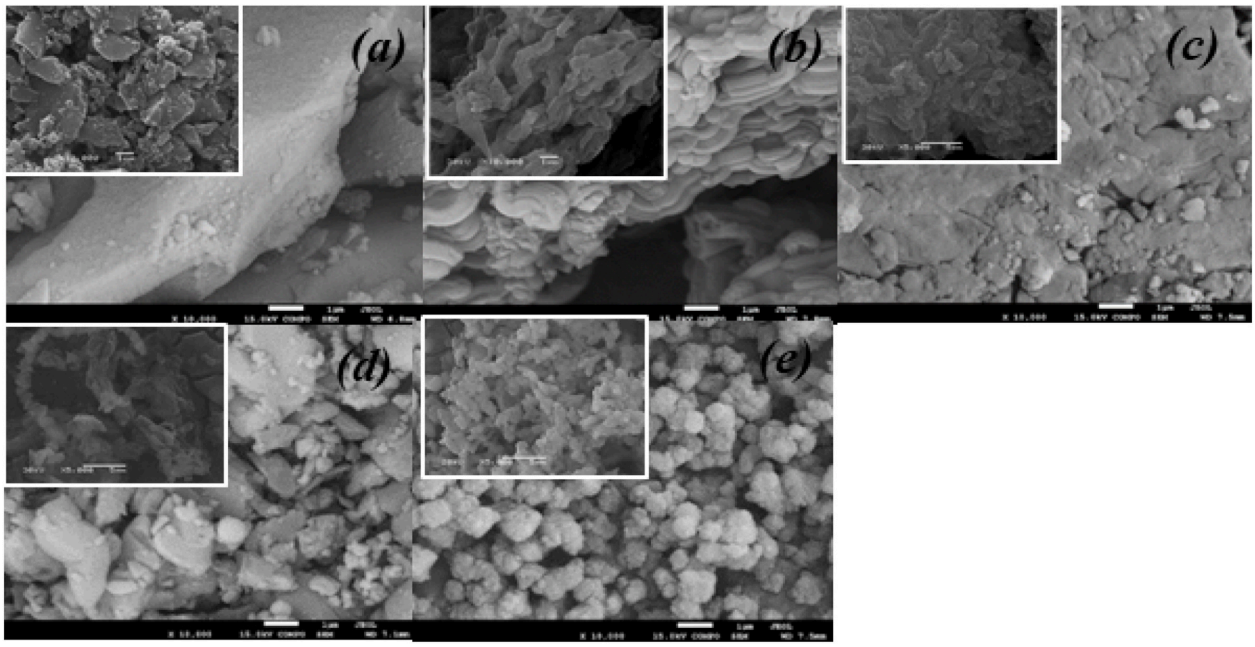

Fig. 3. SEM images of the initial samples (*insert*) and their corresponding Ce-containing derivatives: *SiO_2SO_3H* and *SiO_2SO_3H/Ce (a), SBA* and *SBA/Ce (b), SBA/Ph* and *SBA/Ph/Ce (c), SBA/$PhSO_3H$* and *SBA/$PhSO_3H$/Ce (d), SBA/SO_3H/PO_3H_2* and *SBA/SO_3H/PO_3H_2/Ce (e).*

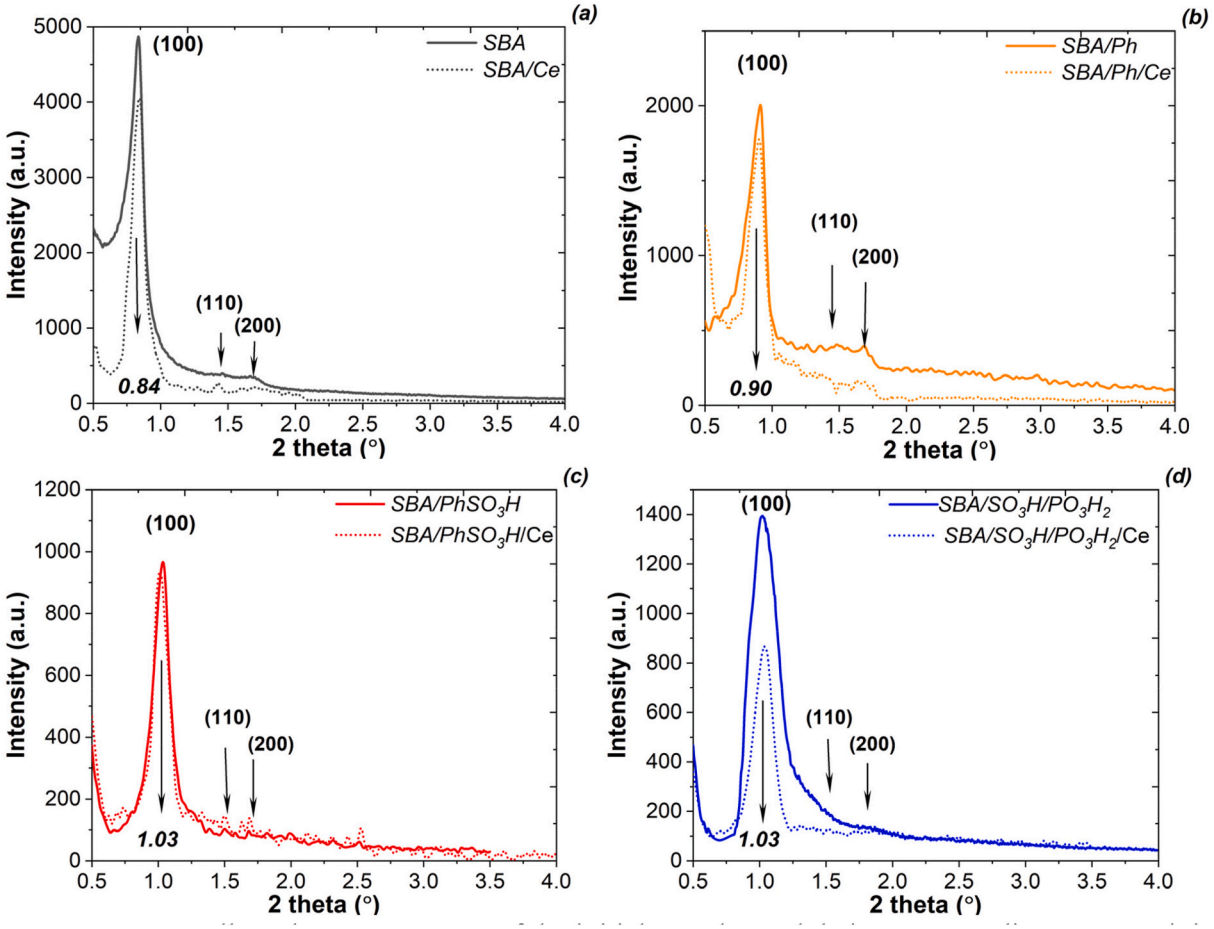

Fig. 4. Small-angle XRD patterns of the initial samples and their corresponding Ce-containing derivatives: *(a) SBA* and *SBA/Ce, (b) SBA/Ph* and *SBA/Ph/Ce, (c) SBA/$PhSO_3H$* and *SBA/$PhSO_3H$/Ce (d) SBA/SO_3H/PO_3H_2* and *SBA/SO_3H/PO_3H_2/Ce.*

unit cell parameters agree well with previously reported values (Table 2). Compared to pristine SBA-15, the organofunctionalized materials exhibited structural changes, specifically reduced d-spacing and thinner pore walls, which is attributed to the influence the volume of the functional groups within the silica framework. It should be noted that the impregnation with Ce^{3+} ions exhibited no effect on the structural parameters of resulted catalysts. The further observations further indicated that the Ce^{3+} impregnation process neither deteriorated the structure of SBA-15 nor led to the formation of a new phase detectable by XRD analysis.

TEM images were used to directly visualize the mesoporous structure of obtained samples and their Ce-containing derivatives (Fig. 5). For the initial samples, the images clearly revealed a well-ordered hexagonal arrangement of lattice fringes, as well as parallel fringes corresponding to a side-on projection of the mesostructure. This observation was in excellent agreement with the XRD results and confirmed that materials possessed a 2D hexagonal mesoporous structure. Importantly, the TEM images of the Ce-containing materials also showed the same ordered hexagonal pattern of mesopores, providing further confirmation that the overall mesostructure was preserved after the impregnation of Ce^{3+} ions.

To confirm the successful and uniform impregnation of Ce^{3+} ions, the EDX analysis was conducted on all Ce-containing catalysts, which verified the uniform distribution of elements throughout the material (Fig. S4). The EDX mapping clearly shows that the cerium species are uniformly distributed across both the internal pore walls and the external surface of the mesoporous support. This effect is likely a direct consequence of the strong interaction between the Ce^{3+} ions and acidic functional groups anchored onto the SBA-15 framework. Consequently, this dual location (internal and external) of the active Ce-centers is critically important for ensuring the observed enhanced catalytic performance, as it significantly increases the accessibility of reactants to the active sites.

EDX analysis was also used to semi-quantitatively assess the chemical composition of the catalysts and compare their elemental content (Table 3). Analyzing these data served to evaluate and confirm the total efficiency of the functionalization of silica and the corresponding metal loading processes.

The amount of impregnated Ce^{3+} ions on the SBA-15 catalysts was determined by analyzing the remaining metal concentration in the solution *via* ICP-OES (Table 3). The quantity of Ce^{3+} ions on the mesoporous SiO_2 surface ranged from 0.41 to 1.69 mmol/g. Pristine SBA-15 exhibited the lowest level of impregnated Ce^{3+} ions, while the catalyst with the greatest number of acidic groups demonstrated the highest level. These results demonstrated a direct correlation between the final Ce^{3+} ions content and the concentration of the acidic functional groups in the samples (Table 2). For the *SBA/SO$_3$H/PO$_3$H$_2$* sample in particular, the amount of Ce^{3+} loaded was measured experimentally to be 1.25 mmol/g. However, the concentration of sulfonic groups alone is only 0.63 mmol/g. This data clearly shows that the sulfonic groups cannot be the sole binding sites, as the measured sorption capacity 1.25 mmol/g is nearly double their concentration 0.63 mmol/g. Furthermore, the total concentration of functional groups (sulfonic and phosphonic) is 2.08 mmol/g, which confirms that metal cations can bind to both sulfonic and phosphonic functional groups. The stoichiometry of the formed complexes, expressed by the ratio C_L: Ce = 2.08 : 1.25, indicates the formation of 1 : 1 and 1:2 complexes (Scheme S1). Thus, for the *SBA/SO$_3$H/PO$_3$H$_2$/Ce* sample, the additional phosphonic groups had no significant impact on Ce^{3+} ion uptake, but rather increased the distribution of incorporated cations through the formation of heteroligand metal complexes.

Table 3
Chemical composition of the obtained samples.

Sample	*EDX analysis*					*Ce loading*, mmol/g*
	O, %	Si, %	S, %	P, %	Ce, %	
SBA/Ce	66.1	31.4	–	–	0.5	0.41
SBA/Ph/Ce	65.3	34.6	–	–	0.1	0.63
SBA/PhSO$_3$H/Ce	63.5	30.7	2.3	–	3.6	1.69
SBA/SO$_3$H/PO$_3$H$_2$/Ce	70.1	25.4	–	4.3	0.2	1.25
SiO$_2$SO$_3$H/Ce	62.9	35.1	0.7	–	1.3	0.51

Notes. *amount of Ce^{3+} ions per gram of the materials according to ICP-OES data.

The high cerium concentration on the *SBA/Ph/Ce* sample, which is almost equivalent to that on *SiO$_2$SO$_3$H/Ce*, can be explained by two primary interactions: electrostatic attraction, which is the general mechanism for all silica-based materials involving attraction between positively charged Ce^{3+} ions and negatively charged regions on the silica surface; and, critically, a π–π interaction. Despite lacking traditional hydroxyl groups, the phenyl groups possess an electron-rich aromatic system whose delocalized π-electrons create a temporary negative polarization that can effectively interact with the positively charged Ce^{3+} ions, thereby stabilizing them on the surface.

To verify the nature of the chemical interactions on the surface of the Ce-impregnated catalysts, FTIR analysis was performed (Fig. 6). The main bands across all samples FTIR spectra were qualitatively similar. The most intense absorption band, observed in the 1076–1095 cm^{-1} range, was attributed to the asymmetric stretching vibration of Si–O–Si bridges. Importantly, a notable redshift of this band compared to pure silica (1200 cm^{-1}) was observed, a phenomenon that the literature attributes to the presence of Si–O–C bridges [42]. Other lower intensity absorption bands were observed at 520 cm^{-1}, 810 cm^{-1}, and 960 cm^{-1}, which were assigned to Si–O–Si deformation, symmetric Si–O–Si stretching, and Si–O–H stretching vibrations respectively. The spectra

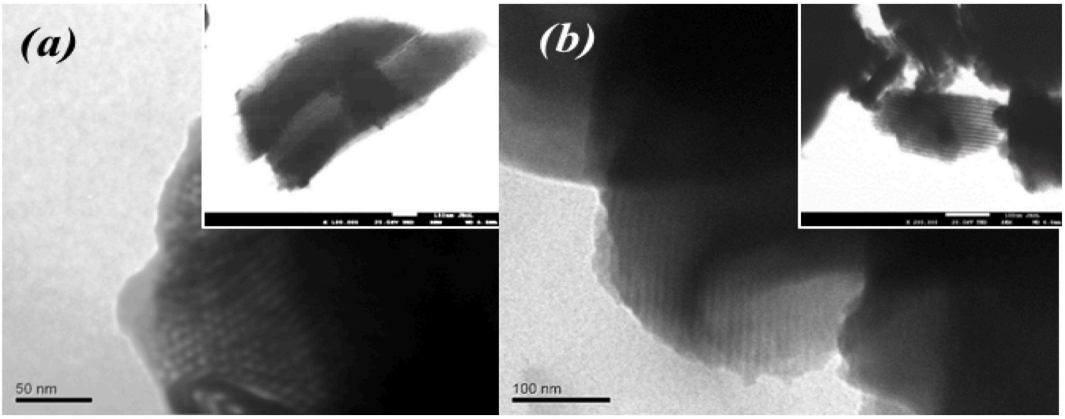

Fig. 5. TEM images of the samples and their Ce-containing derivatives (*insert*): *SBA* and *SBA/Ce (a)* and *SBA/PhSO$_3$H* and *SBA/SO$_3$H/Ce (b)*.

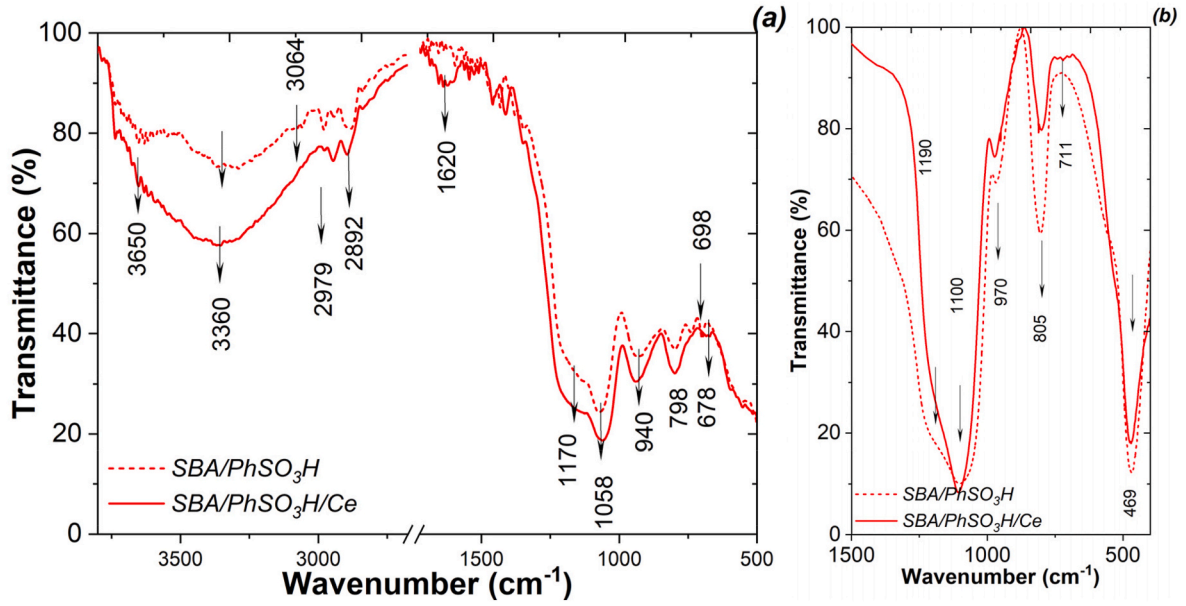

Fig. 6. FTIR spectra of initial and Ce-incorporated samples at room temperature *(a)* and after treatment at 300 °C *(b)*.

also confirmed the presence of various OH-groups. The band at 3745 cm^{-1} corresponds to isolated silanol groups on the external mesopore surface, while the intense, broad band at 3400 cm^{-1} is attributed to hydrogen-bonded Si−OH silanols and adsorbed water molecules. In the spectra of samples functionalized with sulfonic groups and their corresponding Ce-containing derivatives, characteristic bands for the

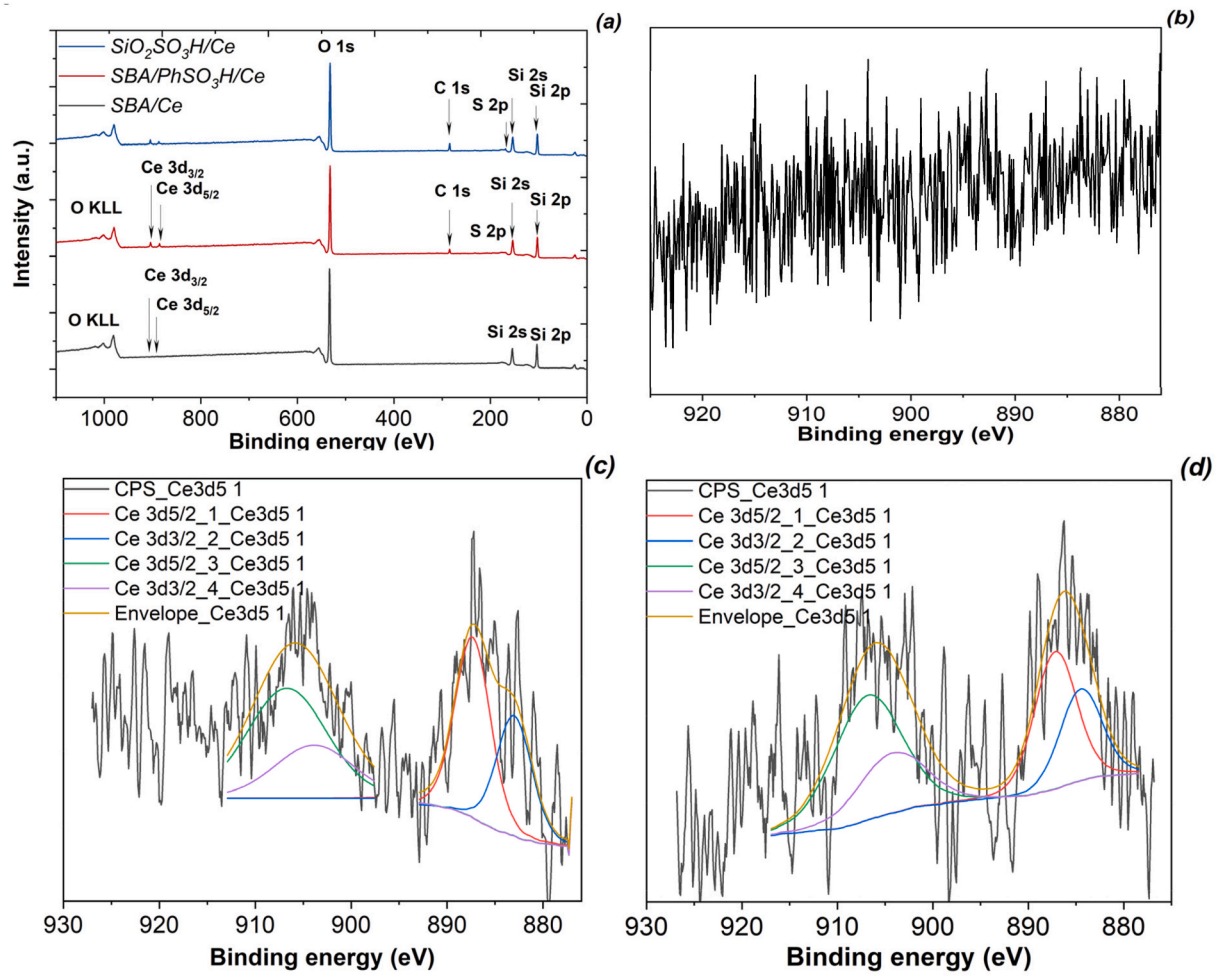

Fig. 7. XPS survey *(a)* and high-resolution spectra for a Ce 3d of *SBA/Ce (b), SBA/PhSO$_3$H/Ce (c)* and *SiO$_2$SO$_3$H/Ce (d)* samples.

functional group spacers were observed. Specifically, the v_{as} of both C-H aryl and C-H alkyl groups appeared at 3030 cm^{-1} and 2930 cm^{-1}, respectively, while the v_s (C-H) bonds was present at 2850 cm^{-1}. Additionally, a band $\delta(C\text{-}H_{alkyl})$ was found at 1465 cm^{-1}. The ν(C=C) vibration was also observed at 1440 cm^{-1}. However, the absorption band of the target sulfonic group (ν(S-O)) at 1070–1020 cm^{-1} falls within the opacity region of the silica matrix. For the Ce-containing samples, the disappearance of the isolated silanol group band at 3750 cm^{-1} indicated an interaction between the silanol groups and the Ce^{3+} ions within the silica matrix. Furthermore, the presence of Ce^{3+} ions significantly increased the intensity of sharp adsorption bands in the 3200−3400 cm^{-1} and 1600−1620 cm^{-1} ranges, which suggested that H_2O molecules served as key complexation ligands. Additionally, a shift of the ν(C=C) band around 1465 cm^{-1} indicated the involvement of the benzene ring in the complexation reaction with Ce^{3+} ions.

The thermal stability of the catalyst's functional layer was further studied by treating samples in vacuum at 200 °C, 250 °C, and 300 °C for 1 h. The spectra of the samples treated between 200 and 250 °C contained the same peaks as those of samples dried at room temperature, indicating that their initial chemical structure was preserved. Decomposition commenced at 300 °C as the material is transformed into other forms. A weak peak at 711 cm^{-1}, which corresponded to the Ce-O bond, provideed evidence for the formation of cerium oxides (Fig. 6b). The observed effect was attributed to the presence of redox-active cerium species, such as Ce^{3+} and Ce^{4+} ions, which could undergo surface oxidation to form the oxide. The results were in excellent agreement with previously published findings for Ce^{3+} ions incorporated into the MCM-41 mesoporous matrix [30].

XPS analysis provided a detailed elemental and oxidation state analysis of the prepared Ce-containing samples (Fig. 7a). XPS survey spectra of the samples confirmed the presence of the silica framework, with core-level peaks for *Si 2p* and *Si 2s* at approximately 103.2 eV and 154.3 eV, respectively, while the O 1s peak was assigned to a binding energy of approximately 533eV. The spectrum of the *SBA/PhSO$_3$H/Ce* sample is characterised by the presence of a C 1s peak at approximately 284.8 eV and a S 2p doublet (2p 3/2 and 2p 1/2) at approximately 168.5 eV. The binding energy of the S 2p peak was characteristic of Sulphur in a highly oxidized state (+6). Similarly, the spectrum of *SiO$_2$SO$_3$H/Ce* sample, with alkylsulfonic groups, also showed clear peaks for C 1s and S 2p, confirming the presence of the -SO_3H functional groups. While the binding energy of the S 2p peak remained consistent with a sulfonic acid group, the intensity and shape of the C 1s and S 2p signals may differ from *SBA/PhSO$_3$H/Ce* sample due to the distinct chemical structure of the ethyl group compared to the phenyl ring, as well as the difference in the base silica material (silica gel vs. SBA-15).

High-resolution XPS spectra of the Ce 3d spin-orbit split components were obtained to characterize the cerium valence states of both the *SBA/PhSO$_3$H/Ce* and *SiO$_2$SO$_3$H/Ce* samples (Fig. 7*)*. For the Ce 3d XPS spectra of *SBA/PhSO$_3$H/Ce* and *SiO$_2$SO$_3$H/Ce*, the typical six peaks of Ce 3d at higher binding energies were observed. The peaks denoted as *v* (882.5 eV), *v'* (889.3 eV), *v''* (898.5 eV), *u* (901.0 eV), *u'* (907.5 eV), and *u''* (916.8 eV) were attributed to Ce^{4+} state [49,50]. In contrast, the Ce^{3+} state was very difficult identified by peaks at lower binding energies, commonly labeled as *v* (880.0 eV), *v'* (885.6 eV), *u* (898.5 eV), and *u'* (903.0 eV). The simultaneous presence of peaks from both the Ce^{4+} and Ce^{3+} oxidation states confirmed that both catalysts existed as mixed-valence systems with strong domination of Ce^{4+} state. Notably, Ce 3d signals were low detected in the *SBA/Ce* sample (Fig. 7b*)*. This observation was primarily because XPS method analyzed only the surface layer of the catalysts. At the same time, the Ce^{3+} ions were also located within the mesoporous channels, which complicated its detection by this method.

It is known [51] that the Ce^{3+} ions are stable in the presence of O_2 in the low pH range (pH < 2). Therefore, O_2 may not oxidise Ce^{3+} to Ce^{4+} within this pH range. However, at higher pH values, Ce^{3+} ions can be oxidized to $Ce(OH)_4$ by O_2. This pH range depends on the concentration of Ce^{3+}. It is pH 4.3 at $[Ce^{3+}] = 1$ and pH < 6.3 at $[Ce^{3+}] = 10^{-6}$ M. At higher pH values (pH > 4), O_2 tends to oxidise Ce^{3+} to Ce^{4+}, primarily producing $Ce(OH)_2^{2+}$, $Ce(OH)_4$ and $CeO_2{\cdot}xH_2O$, in line with the following reactions: $Ce^{3+} + 4H_2O \rightarrow Ce(OH)_4 + 4H^+ + e-$, $4Ce^{3+} + O_2 + 6H_2O \rightarrow 4Ce(OH)_2^{2+} + 4H^+$, $4Ce(OH)_2^{2+} \xrightarrow{O_2} CeO_2\downarrow + 2H^+$ and $4Ce^{3+} + O_2 + 6H_2O \rightarrow 4CeO_2\downarrow + 12H^+$.

The successful preparation of CeO_2 on the surface of the samples was further confirmed by the appearance of new absorption bands at 255 nm and 368 nm in the diffusion reflectance spectra, located in octahedral and tetrahedral coordination environments, respectively, which were not present in the initial samples (Fig. 8a). Also, a spectral redshift in the absorption edge was evident in the spectra obtained for samples containing a high concentration of Ce^{3+} ions (Table 3), and it was especially evidenced by the *SBA/SO$_3$H/PO$_3$H$_2$/Ce*, as compared to the *SBA/Ce* spectrum. The red shift effect observed in functionalized materials may be attributed to the formation of localized states within the band gap, which was caused by an increase in the concentration of Ce^{3+} ions due to oxygen vacancies. The band gap energies of samples were quantified from the Tauc plots (Fig. 8b). The E_g values for the *SBA/Ce*, SBA*/Ph/Ce, SiO$_2$SO$_3$H/Ce,* SBA*/PhSO$_3$H/Ce,* and *SBA/SO$_3$H/PO$_3$H$_2$/Ce* samples were obtained as 2.99 eV, 2.98 eV, 2.97 eV, 2.96 eV and 2.95 eV, respectively. The energy levels exhibited by the samples deviated from the archetypal E_g value of cerium oxide (~3.2 eV [49]). Nevertheless, the decrease in the band gap observed in the samples was directly linked to an increase in the concentration of Ce^{3+} ions (Table 3) and a corresponding reduction in the size of the CeO_2 particles at the nanoscale [18]. This phenomenon could be successfully explained by the ordered structure of the SBA-15 matrix, which confined and limited the growth of CeO_2 within the mesopores [30]. The bands of spectra were assigned to the presence of CeO_2 nanoparticles although the crystallites escaped the XRD detection [52].

TGA analysis was used to investigate the thermal stability of the obtained materials, in order to determine their suitability for catalytic activity across temperature range**.** Thermal analysis of the initial organo-functionalized silica revealed four distinct thermal events (Fig. S3), which occurred sequentially across a broad temperature range:

(1) evaporation of physically adsorbed water (endothermic, from room temperature up to 150 °C);
(2) the initial decomposition of surface organic groups (exothermic, from 250 °C to 400 °C), corresponding to the breakdown of carbon chains and subsequent generation of alkenes, CO_2 and SO_2 (>350 °C);
(3) decomposition of organic residues (exothermic from 350 °C to 550 °C), reflecting the bulk thermal degradation of the remaining template and residual organic species;
(4) condensation of isolated silanol groups (endothermic, from 500 °C to 1000 °C), typically exhibiting very weak or almost undetectable signals in the DTG curve.

The thermal decomposition process of the Ce-containing catalysts was also studied (Fig. 9). As the catalyst matrix (SiO_2) is thermally inert, thermochemical analysis provided an accurate estimation of the functional layer composition. For the *SBA/Ce* sample, only an endothermic effect was observed in the temperature range from 20 to 150 °C for physically adsorbed water release (10.0 %). In the temperature range of 200–650 °C, a clear exothermic peak was observed at 500 °C for the *SBA/PhSO$_3$H/Ce* sample, accompanied by significant mass loss (9.5 %). At the same time, the bifunctional catalyst (*SBA/SO$_3$H/PO$_3$H$_2$/Ce*) exhibited a more complex thermal profile, displaying two exothermic events at 350 °C and 550 °C of varying intensity, which contributed to mass losses of 11.6 % and 7.5 %, respectively. These effects confirmed the separate thermal degradation of two types of functional organic groups that were covalently bounded in the silica surface, including the degradation of corresponding complexes to cerium oxides. For

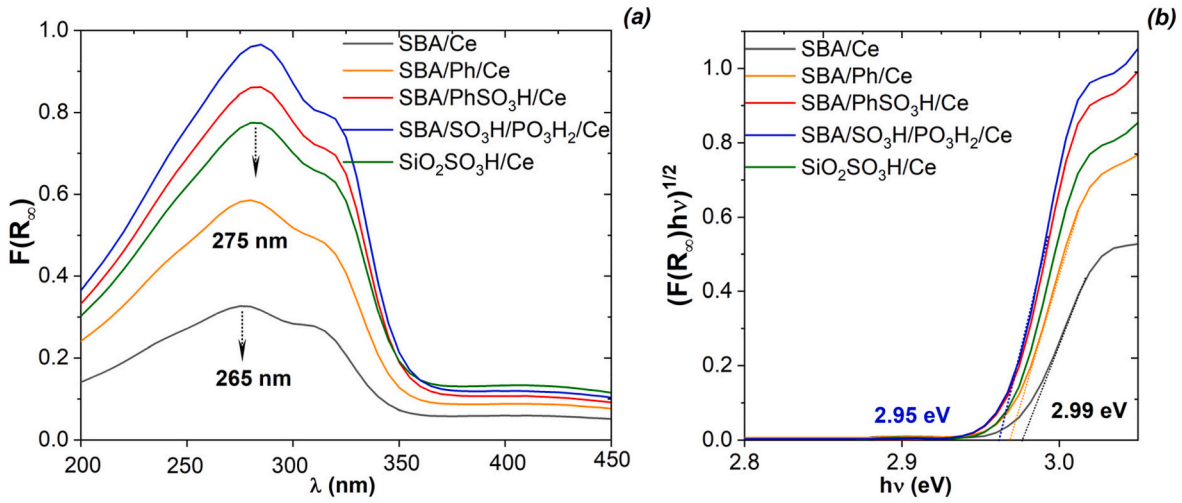

Fig. 8. Diffuse reflectance spectra *(a)* and their corresponding Tauc plots *(b)* for *SBA/Ce*, SBA/*Ph/Ce*, SBA/*PhSO₃H/Ce*, *SBA/SO₃H/PO₃H₂/Ce* and *SiO₂SO₃H/Ce* samples.

SiO₂SO₃H/Ce, the exothermic effect was practically invisible because no significant mass loss was observed at temperatures between 150 °C and 500 °C. Thus, the metal incorporation significantly enhanced their thermal stability (up to 400 °C) compared to the initial, unmodified samples. This is due to the strong coordination between the Ce^{3+} ions and the functional groups on the silica surface, particularly the phenolic and sulfonic groups. This interaction helped to anchor and stabilize these groups, preventing their premature thermal degradation or decomposition. Consequently, the catalyst retained its structural integrity and functional properties at elevated temperatures, which was essential for its performance in the ethanol dehydration reaction.

The intrinsic acidity of the prepared catalysts was tested by measuring the adsorption of a basic probe, such as pyridine. The DRIFT spectra of pyridine adsorbed at 150 °C on the initial and Ce-containing samples are shown in Fig. 10.

The DRIFT spectra identify the two primary types of acid site based on their characteristic absorption bands: (a) Brønsted acid sites, represented by the PyH^+ ion; the C–C stretching of the pyridinium ion, formed by proton transfer from a Brønsted acid sites, appears at around 1540 and 1640 cm^{-1}. These are typically strong sites arising from the H^+ of sulfonic or phosphonic groups on the silica surface; and (b) Lewis acid sites, represented by pyridine coordinated to metal cations or surface defects. These correspond to peaks at 1450 cm^{-1} and a combined peak at around 1447–1460 cm^{-1}. Pristine SBA materials exhibits minimal acidity in the 1400–1700 cm^{-1} range. The Lewis acid sites are originated from siloxane bridges (Si–O–Si) and silanols (Si–OH) on the SiO_2 surface was also presents. Ce-containing samples exhibit a clear and significant increase in the intensity of the L-acid peaks (~1450 cm^{-1}) compared to the initial samples. This confirms that the incorporated Ce species, such as Ce^{3+} ions or CeO_2 nanoparticles, act as effective Lewis acid centers, which are crucial for activating molecules such as ethanol in the catalytic cycle.

The IR peaks due to pyridine decreased after treatment at an increased temperature up to 450 °C on Brønsted acid centers, whereas there was little change at this temperature on Lewis acid sites (Fig. S5), suggesting that Lewis acid sites are stronger at high temperatures on Ce-containing catalysts than Brønsted acid centers. High concentration of Ce-sites in *SBA/PhSO₃H/Ce* sample leads to a higher concentration of Ce-pyridine complexes at 450 °C also compared with other samples. The ready accessibility of both Brønsted and Lewis acid sites on the *SiO₂/SO₃H/Ce* catalyst contributes to its high intrinsic efficiency per active site, even after thermal treatment.

3.2. Catalytic activity

3.2.1. Catalytic performance of Ce-containing materials

The catalytic activity of the obtained mesoporous materials was tested in the ethanol dehydration reaction at mid-to-high temperatures. Ethanol dehydration over obtained mesoporous catalysts chiefly produced C_2H_4, CH_3CHO and $C_2H_5OC_2H_5$, with trace amounts of H_2, CH_4, CO_2 etc. The dependence of ethanol conversion, yield and selectivity to products (ethylene and acetaldehyde) on the reaction temperature was calculated for each catalyst (Fig. 11).

As shown in Fig. 11, the catalytic performance of the studied samples was depended on both their chemical composition and the reaction temperature. Increasing the reaction temperature to 500 °C led to a substantial enhancement in the conversion of ethanol from 20 % to 95 % over the studied catalysts (Fig. 11a). Furthermore, it was evident that ethylene was the predominant product. The ethylene yield was found to be less than the amount of ethanol that was converted, due to the presence of by-products in the reaction (Fig. 11b). *SBA/PhSO₃H/Ce* exhibited the highest catalytic activity for ethanol conversion (95 %) within the studied temperature range, exhibiting the highest yield of C_2H_4 among all obtained catalysts. The *SBA/SO₃H/PO₃H₂/Ce* catalyst was less effective at ethanol conversion (65 %) than the *SBA/PhSO₃H/Ce* catalyst. Concurrently, *SBA/Ph/Ce* exhibited lower catalytic activity in comparison to *SBA/PhSO₃H/Ce* and *SBA/SO₃H/PO₃H₂/Ce* samples. The yield of ethylene gradually grew with the increase of reaction temperature, while the yield of acetaldehyde slowly increased up to 425 °C to reach the plateau of about 24 %. The catalytic behavior of *SBA/Ph/Ce* catalyst was very similar to *SBA/Ce*, however it was the least active catalyst in the series studied. Again, the gradual growth of ethylene and acetaldehyde yield with the reaction temperature was observed. The catalytic behavior of the *SiO₂SO₃H/Ce* catalyst was very similar to the *SBA/PhSO₃H/Ce* catalyst, exhibiting good catalytic activity for ethanol conversion (79 % at 500 °C) in all studied temperature range. However, the *SBA/PhSO₃H/Ce* catalyst was slightly more selective toward formation of C_2H_4 (68.3 %). The yields of ethylene and acetaldehyde increased with rising reaction temperature for both catalysts, but the yield ratio of the two products was observed differently. Therefore, the acidic center plaid a crucial role in the conversion of ethanol to C_2H_4.

From the product selectivity presented in Fig. 11c, it was clear that the *SBA/SO₃H/PO₃H₂/Ce* catalyst was able to dehydrate ethanol with an impressive ~99 % selectivity toward ethylene at 250−275 °C. For ethanol dehydration at 250 °C, industrially used commercial γ-Al_2O_3 displays ethanol conversion of 85 % and ethylene selectivity of 16 % [21]. In contrast, at this temperature, other SBA-15-type catalysts

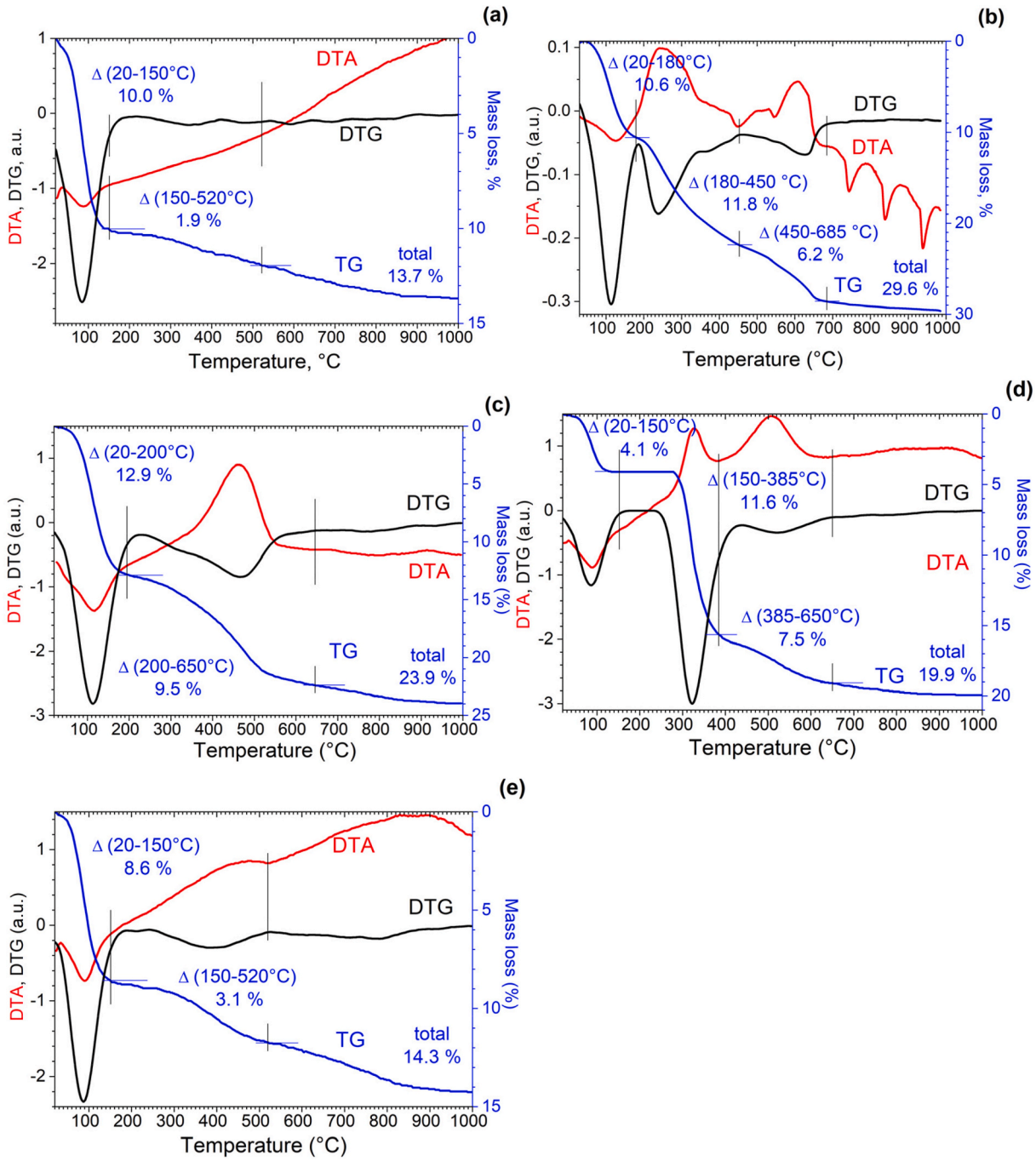

Fig. 9. TGA analysis of Ce-containing samples: *SBA/Ce (a), SBA/Ph/Ce (b), SBA/PhSO$_3$H/Ce (c), SBA/SO$_3$H/PO$_3$H$_2$/Ce (d)* and *SiO$_2$SO$_3$H/Ce (e)*.

showed only 1–2 % ethylene selectivity. Although the mesoporous catalysts demonstrated lower activity at low temperatures, the ethylene selectivity at 500 °C was high, following the order: *SBA/SO$_3$H/PO$_3$H$_2$/Ce* > *SBA/PhSO$_3$H/Ce* > *SiO$_2$SO$_3$H/Ce* > *SBA/Ph/Ce* > *SBA/Ce*. Although *SBA/PhSO$_3$H/Ce* catalyst exhibited a high concentration of Ce^{3+} ions (Table 3), primarily attributed to the electrostatic attraction between the Ce^{3+} species and the phenolic groups [42]. Furthermore, increasing the coverage of the functional phenyl sulfonic groups enhanced Ce^{3+} ions, confirming that the sulfonic groups were the main binding sites. Ultimately, the presence of these bifunctional S-, P-, and O-donor ligands enabled both a high overall metal uptake and a more uniform distribution of the Ce^{3+} ions across the *SBA/SO$_3$H/PO$_3$H$_2$/Ce* catalyst surface. Thus, the enhanced catalytic activity, evidenced by the relatively high ethanol conversion, ethylene yield, and selectivity, was a direct result of the increased Ce^{3+} ions content and its uniform distribution on the silica surface, combined with a high redox function (Ce^{3+}/Ce^{4+} ion pairs).

When using the *SBA/Ce* and *SiO$_2$SO$_3$H/Ce* catalysts, the acetaldehyde yield increased slowly from 0.5 to 27.6 % and from 0.1 % to 38.2 % with increasing reaction temperatures up to 500 °C, respectively (Fig. 11d). Thus, the acetaldehyde yield profiles for the *SiO$_2$SO$_3$H/Ce* and *SBA/Ce* samples were found to be qualitatively similar. In contrast, for other catalysts, this behavior stabilized at 25 % at high temperatures (>300 °C). Furthermore, the *SBA/SO$_3$H/PO$_3$H$_2$/Ce* catalyst produced the lowest acetaldehyde yield of all the catalysts that were tested. This indicates that, in this case, the role of the redox function was more significant than that of the acidic function in determining these yield profiles (Fig. 11e).

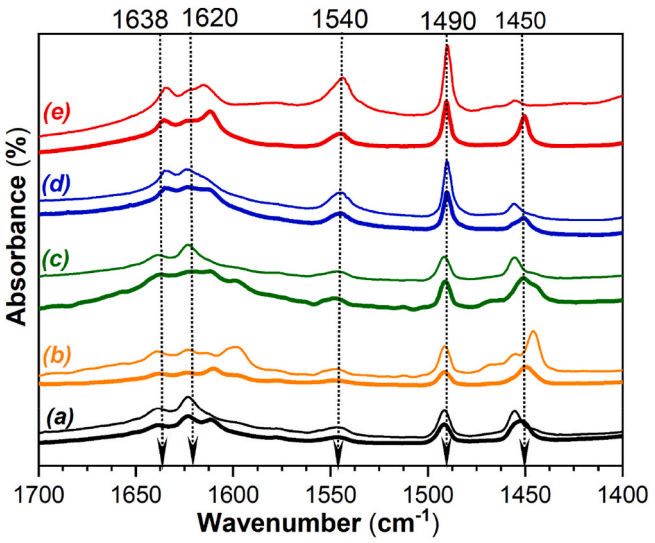

Fig. 10. DRIFT spectra (pyridine region) of adsorbed pyridine at 150 °C on the initial samples and their corresponding Ce-containing derivatives: *(a) SBA* and *SBA/Ce, (b) SBA/Ph* and *SBA/Ph/Ce, (c) SBA/PhSO$_3$H* and *SBA/PhSO$_3$H/Ce, (d) SBA/SO$_3$H/PO$_3$H$_2$* and *SBA/SO$_3$H/PO$_3$H$_2$/Ce.*

With the exception of the *SBA/SO$_3$H/PO$_3$H$_2$/Ce* sample, the synthesized silica-based catalysts generally exhibited significantly lower catalytic activity for ethanol dehydration when tested at lower reaction temperatures (Fig. 12a). The catalytic performance for all samples improved proportionally with the rise in temperature (Fig. 12b). Specifically, the reaction conducted at 500 °C yielded the most prominent results compared to experiments performed at all other lower temperatures.

3.2.2. Kinetic studies

The kinetic parameters, especially the activation energy (E_a), are critical and highly informative metrics for quantitatively evaluating the catalytic efficiency of various functionalized silica-based catalysts. Assuming that this process was described by a first-order kinetic reaction, the E_a values for the Ce-containing catalysts were calculated using Arrhenius equation ($K = Aexp\left(-E_a/RT\right)$). These values for all solid acid catalysts are listed in Table 4.

For all samples, the rate constants demonstrate a clear, exponential increase with temperature, confirming the thermal activation required for ethanol dehydration (Table 4). The highest overall rate constants and the lowest activation energies were achieved over the *SBA/PhSO$_3$H/Ce* and *SiO$_2$SO$_3$H/Ce* catalysts compared to the other investigated materials. The low E_a values for these catalysts suggest that the strong acidity introduced by the sulfonic groups, which complex the Ce^{3+}ions, creates the most favourable transition state environment, resulting in the highest measured rate constants at 500 °C. Given that Brønsted acidic groups possibly undergo rapid deprotonation or degradation at temperatures up to 500 °C, the remaining Lewis acid sites are likely the dominant active species at high temperatures. Therefore, *SBA/PhSO$_3$H/Ce* superior overall catalytic performance is primarily driven by its high concentration of accessible active sites and strong acid promotion, which lowers E_a, rather than the exceptional intrinsic efficiency of individual Ce centers. Interestingly, the *SiO$_2$SO$_3$H/Ce* catalyst achieves the highest TOF (1.451 s^{-1} at 500 °C) and consequently the highest TON (5223.6 per hour), suggesting that the active centers of the *SiO$_2$SO$_3$H/Ce* catalyst are the most accessible and efficient on a per-site basis, likely due to optimal dispersion and minimal site blocking on the surface. On other hand, the *SBA/SO$_3$H/PO$_3$H$_2$/Ce* sample generally exhibits only medium activity, in terms rate constants and TOF/TON, across all temperatures, which may be indicative of severe steric hindrance or strong product/reagent poisoning, given its complex multi-functionalization. Finally, the *SBA/Ce* catalyst exhibits the highest E_a (68.5 kJ/mol), confirming that the simple Ce-loaded support is the least efficient from a catalytic perspective.

3.2.3. Reaction mechanism

Ethanol conversion over Ce-impregnated acid functionalized silica catalysts proceeds *via* a multi-functional mechanism including Brønsted (B) and Lewis (L) acid sites, significantly lowering the E_a compared to the non-catalytic route (Scheme 1). The reaction begins with the

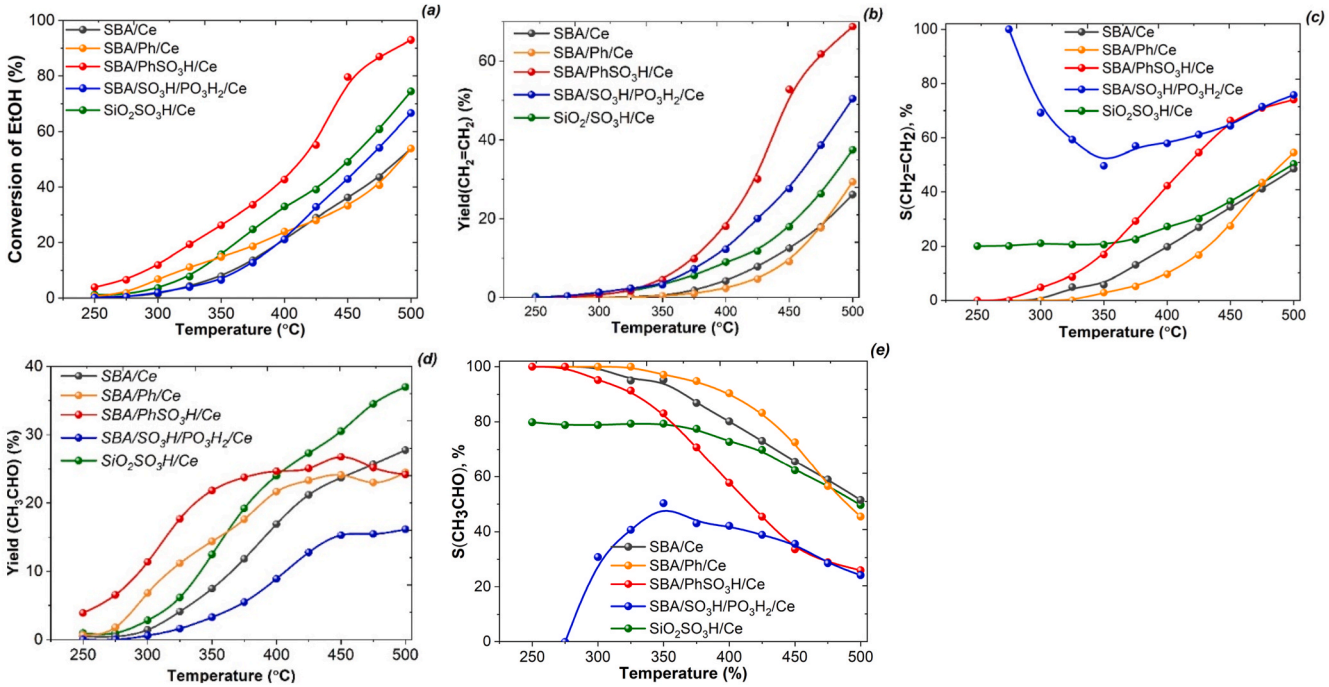

Fig. 11. Effect of temperature on the ethanol conversion (*a*), yield *(b, d)* and selectivity *(c, e)* to products over obtained catalysts.

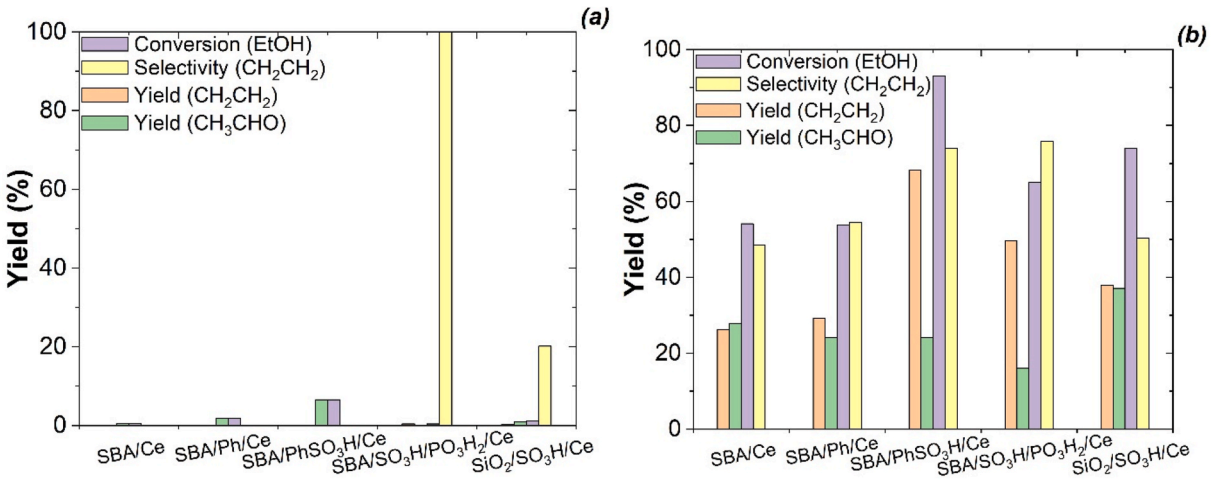

Fig. 12. Comparison of catalytic activity of synthesized materials at 275°C *(a)* and 500 °C *(b)*.

Table 4
Kinetic parameters for ethanol dehydration with Ce-containing catalysts.

Sample	T, °C	K 10^{-4}, L/mol·s	E_a, kJ/mol	TOF, s^{-1}	TON	$F_{C_2H_4}/W \cdot 10^5$, *mol/g·s*
SBA/Ce	250	0.0305	68.5	0.073	262.8	0.00
	300	0.0943		0.220	792.0	0.00
	350	0.1984		0.439	1580.4	0.03
	400	0.3980		0.805	2898.0	0.08
	450	0.6931		1.220	4392.0	0.16
	500	1.0498		1.585	5706.0	0.35
SBA/Ph/Ce	250	0.0408	65.1	0.063	226.2	0.00
	300	0.1054		0.159	572.4	0.01
	350	0.2614		0.365	1314.0	0.07
	400	0.5108		0.634	2286.0	0.18
	450	0.9163		0.952	3427.2	0.45
	500	1.3863		1.19	4284.0	0.83
SBA/PhSO$_3$H/Ce	250	0.0408	48.2	0,024	86.4	0.00
	300	0.1863		0.101	363.6	0.05
	350	0.4308		0.207	745.2	0.53
	400	0.7985		0.325	1170.0	1.87
	450	1.5606		0.467	1681.2	5.14
	500	2.6593		0.550	1980.0	6.88
SBA/SO$_3$H/PO$_3$H$_2$/Ce	250	0.0100	56.0	0.008	17.28	0.00
	300	0.0513		0.040	86.4	0.00
	350	0.1984		0.144	311.4	0.23
	400	0.4308		0.280	605.9	0.98
	450	0.8440		0.456	986.4	3.71
	500	1.1394		0.544	1177.2	5.00
SiO$_2$SO$_3$H/Ce	250	0.0407	54.8	0.078	280.8	0.00
	300	0.1165		0.216	777.6	0.02
	350	0.3147		0.529	1904.4	0.14
	400	0.6163		0.902	3247.2	0.32
	450	1.1394		1.333	4798.8	2.38
	500	1.3471		1.451	5223.6	3.89

Notes. K – rate constant; *TOF* – turnover frequency; *TON* – turnover number; $F_{C_2H_4}/W$ – reaction productivity.

protonation of C_2H_5OH by strong Brønsted acid sites (a process that is particularly well optimized on the *SBA/PhSO$_3$H/Ce* sample), forming a highly reactive oxonium ion intermediate, which then determines the product pathway: (1) it either undergoes intermolecular attack by a second ethanol molecule to form DEE (preferred at low temperatures), or (2) it undergoes intramolecular dehydration and subsequent deprotonation *via* an ethylcarbocation to form C_2H_4, the dominant pathway at temperatures above 350 °C. At the same time, the Ce^{3+}/Ce^{4+} species exhibit a high oxygen storage capacity, providing redox centers that facilitate the parallel oxidative pathway. The functionalized groups play a crucial role in enhancing catalytic efficiency by controlling acidity, which leads to more controlled dispersion of Ce^{3+}/Ce^{4+} sites and prevents the formation of large, catalytically inactive agglomerates (a process that is particularly well optimized on the *SiO$_2$/SO$_3$H/Ce* sample). Specifically, the functionalized *-SO$_3$H* and *-P(O)(OH)$_2$* groups (as seen in the *SBA/SO$_3$H/PO$_3$H$_2$/Ce* sample) serve a dual purpose: (1) they create coordination sites that significantly improve the incorporation and uniform dispersion of Ce^{3+}/Ce^{4+} sites, and (2) provide the strong B-acidity necessary to achieve the lowest E_a for efficient C_2H_4 production across a wide temperature range. This structural and acidic fine-tuning is consistent with the varied observed catalytic characteristics of the *SBA/PhSO$_3$H/Ce*, *SiO$_2$/SO$_3$H/Ce* and *SBA/SO$_3$H/PO$_3$H$_2$/Ce* samples in the ethanol dehydration reaction.

3.2.4. Comparison of the catalytic activity with previously reported solid catalysts

The obtained catalysts were comprehensive compared with previously reported materials for the dehydration of ethanol to ethylene (Table 5). The *SBA/PhSO$_3$H/Ce* sample demonstrated superior performance at 500 °C, achieving approximately 95 % ethanol conversion and 68 % ethylene yield, which significantly surpassed the typical conversion (~60 %) and lower selectivity generally reported for unsupported or simply modified CeO_2 systems under identical conditions (e.g., H_3PO_4-modified CeO_2 and other ceria formulations which reach conversion in the range of ~60 % at similar temperatures and lower ethylene selectivity [10,14]). Nevertheless, strongly acidic microporous zeolites (e.g., optimized ZSM−5) remained superior in achieving near-quantitative ethylene yield and selectivity at markedly lower temperatures. Consequently, differences in feed concentration and reactor configuration must be considered when comparing absolute numbers [19,31]. Optimized ZSM-5 catalysts (dealuminated and acid-tuned) were demonstrating high ethylene selectivity (~100 %) and yield (~98–99 %) [22] at low temperature (~220 °C) with concentrated ethanol feed and optimized weight hourly space velocity. Although these materials were superior for maximising ethylene yield and operating at low temperatures, they differed fundamentally from mesoporous SBA-15 in terms of their pore structure, acid density/strength and coking tendencies. Therefore, the *SBA/SO$_3$H/PO$_3$H$_2$/Ce* and *SBA/PhSO$_3$H/Ce* catalysts were promising alternatives that were more cost-effective and less prone to coking, although they have not yet achieved the same level of selectivity as optimized ZSM-5 [22].

3.2.5. Reusability and characterization of spent catalysts

The most critical factors influencing the practical application and long-term economic viability of solid acid catalysts are catalyst deactivation and recyclability [29]. To assess the stability of the prepared materials, catalyst deactivation was tested at 200–500 °C for a duration

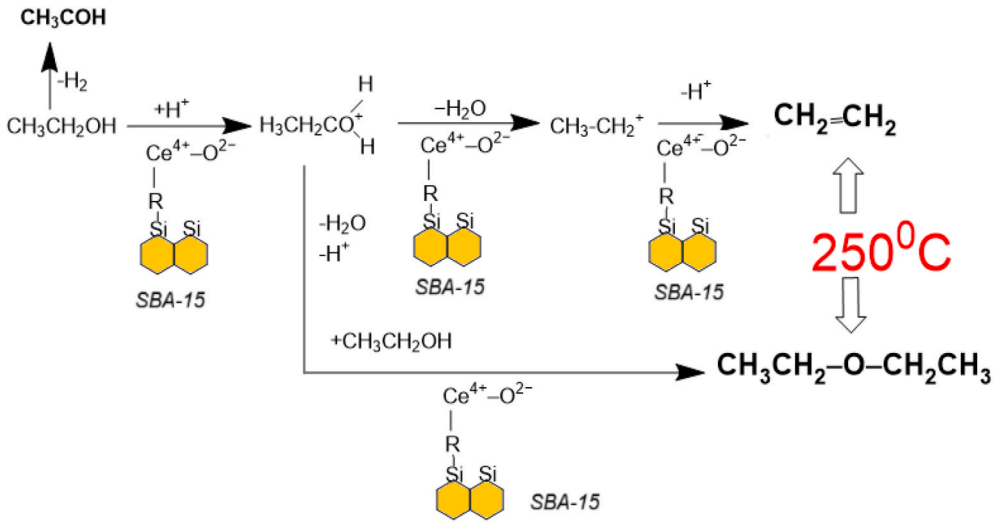

Scheme 1. Simplified mechanistic pathways for ethanol dehydration with obtained SBA-15 catalysts.

Table 5
Summary of catalysts used for the dehydration of ethanol to ethylene and their catalytic parameters.

Catalyst	T (°C)	Conversion of ethanol (%)	Selectivity of ethylene (%)	Major by-products	Ref
TiO_2/γ-Al_2O_3	500	95.0–99.96	96–99.34	DEE	[8]
CeO_2 (unmodified)	~500	~7	~50	DEE, acetaldehyde	[14]
CeO_2	~500	~10	59.74	DEE, acetaldehyde	[10]
$30H_3PO_4$-CeO_2		~60	~99		
La15/CeO_2	450	63	~47	Acetaldehyde, CO, CO_2	[19]
WO_3/silicate	200	70	99	–	[17]
HZSM-5	300	95.0–99.0	60	DEE (13 %), unknown higher hydrocarbons (14 %)	[21]
Rho zeolite	300	100	99		
HZSM-5	275	98.5	~98.6	Minor coke	[22]
ZSM-5-deAl-1/100	240	98.9	99.9		
ZSM-5-P	240	99.8	94.4		
ZSM-5-La	240	97.7	93.3		
Cu/MCM-41	300	50	–	Selectivity of acetaldehyde (100 %), Selectivity of ethyl acetate (20 %)	[27]
Palm oil clinker derived SBA-15	400	~73	~85	DEE (lower T)	[31]
SiO_2SO_3H/Ce	500	79	55	DEE (lower T), minor acetaldehyde	this
SBA/SO_3H/PO_3H_2/Ce		65	79		work
SBA/$PhSO_3H$/Ce		95	73		

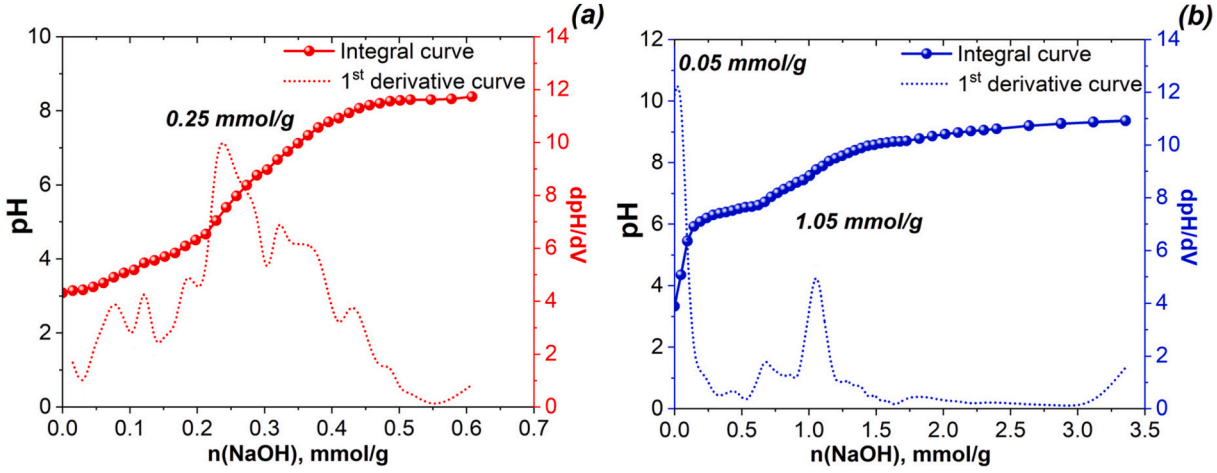

Fig. 13. Potentiometric titration curve and corresponding first derivative curve of the spent *SBA/$PhSO_3H$/Ce (a)* and *SBA/SO_3H/PO_3H_2/Ce (b)* catalysts.

of 1 h. The results confirmed that the conversion remained highly stable for the prepared samples throughout this period. All tested catalysts did not exhibit any change of colour, which strongly indicates the absence of coke formation on the catalyst surface after the catalysis experiments.

The used catalysts were characterized using FTIR analysis and total acidity calculations. Specifically, the acidity of the spent *SBA/PhSO$_3$H/Ce* and *SBA/SO$_3$H/PO$_3$H$_2$/Ce* catalysts was evaluated following use *via* the acid-base titration method (Fig. 13). Analysis revealed a significant decrease in surface acidity for both materials. The concentration of acidic groups (number of active H^+ sites) of spent catalysts was found to be around 0.25 mmol/g for the *SBA/PhSO$_3$H/Ce* and 1.05 mmol/g for the *SBA/SO$_3$H/PO$_3$H$_2$/Ce*, which was consistent with the initial measured pH values of 3.08 and 3.2, respectively. Based on these results, the sharp reduction in quantified acidic sites was due to the deactivation of the spent catalysts, which was directly attributable to the partial leaching of sulfonic groups from the surface during ethanol dehydration.

The FTIR spectrum of the spent bare catalyst (*SBA/Ce* sample) exhibited three characteristic Si−O−Si peaks centered at 1100 cm^{-1}, 770 cm^{-1}, and 450 cm^{-1} (Fig. S7a). Furthermore, a broad envelope centered at approximately 3440 cm^{-1} was attributed to the surface OH stretching vibration, and a peak at 3560 cm^{-1} was assigned to the bending vibration of non-condensed Si−OH groups. Critically, the spectrum showed no detectable bands corresponding to ν(Ce−O) vibration, which strongly indicated the complete loss or significant leaching of Ce^{3+}/Ce^{4+} species from the surface of this catalyst after use. The intensity of the Si−OH-related features decreased in the Ce-containing organofunctionalized catalysts (Fig. S7b and c), a change that was sustained after catalysis due to the initial substitution of surface silanols by phenyl and propyl silane groups. The spectra confirmed the continued presence of the organic structure through peaks attributable to C−H stretching (2974–2893 cm^{-1}) and skeletal vibrations (1600–1400 cm^{-1}). Typically, the $-SO_3^-$ symmetrical and asymmetrical vibrational modes (at 1060 and 1125 cm^{-1}) occurred at higher wavenumbers than the main silica network modes (1190–1160 cm^{-1}). Importantly, FTIR spectra of both *SBA/PhSO$_3$H/Ce* and *SBA/SO$_3$H/PO$_3$H$_2$/Ce* clearly showed bands corresponding to the ν(Ce−O) vibration at 710 cm^{-1}, indicating that CeO_2 remained robustly anchored on the surface of these organofunctionalized catalysts after use.

The stability assessment confirmed that the prepared Ce-containing catalysts exhibited excellent thermal and structural stability, maintaining stable ethanol conversion throughout the 1 h test at 200–500 °C. However, post-reaction analysis revealed that subsequent catalyst deactivation, observed as a sharp reduction in quantified acidic sites, was directly attributable to partial leaching of sulfonic groups from the surface during ethanol dehydration. This finding highlights the need to stabilize the organic functional groups on the mesoporous silica support for further to maximise catalyst lifetime.

4. Conclusions

For the first time, highly efficient mesoporous solid acid catalysts based on SBA-15 and amorphous SiO_2, which are functionalized with Brønsted acidic groups (-SO_3H and -PO_3H_2) and Lewis acidic/redox active species were reported for the selective conversion of ethanol. The influence of the Ce^{3+} cations included in the various silicas functionalized with acid groups on their catalytic behaviour in the ethanol dehydration reaction was investigated. The catalysts were evaluated across a wide temperature range (250–500 °C), demonstrating high ethylene yields at reduced temperatures, making them a promising and economically viable alternative for industrial-scale bioethylene production. The key factor influencing the catalytic performance were the interactions between Ce^{3+} ions and the functional groups on the mesoporous support. The dispersion of cerium within the SBA-15 silica matrix directly affected the surface acidity of the catalysts. Experimental results showed that the phenylsulfonic-functionalized sample exhibited the highest catalytic activity. Ethanol conversion and yield to ethylene increased with rising the reaction temperature. Strong acidic properties were a key factor for high activity (*SBA/PhSO$_3$H/Ce, SBA/SO$_3$H/PO$_3$H$_2$/Ce*). The redox function was more important at lower temperatures, especially for *SiO$_2$SO$_3$H/Ce* and *SBA/Ce*. Catalysts *SBA/Ph/Ce-SBA/SO$_3$H/PO$_3$H$_2$/Ce* showed transitions in function dominance depending on temperature, which can be critical for controlling the selectivity (ethylene vs acetaldehyde). Thus, the ethanol dehydration reaction served as an effective probe for the simultaneous assessment of the acidic and redox functions of solid catalysts.

CRediT authorship contribution statement

Oksana Dudarko: Writing – original draft, Methodology, Investigation, Funding acquisition, Conceptualization.

Declaration of competing interest

The authors declare that they have no known competing financial interests or personal relationships that could have appeared to influence the work reported in this paper.

Acknowledgment

Authors are grateful to the project “Multifunctional hybrid adsorbents for water purification" supported by the Swedish Research Council (Vetenskapsrådet) Swedish Research Program, Dnr. 2018–2021 and NAS-PAN joint project (2018–2020). Thanks to the 2nd European Chemistry School for Ukrainians for their invaluable support. The authors are indebted to Fredric G. Svensson for the XPS measurements.

Appendix A. Supplementary data

Supplementary data to this article can be found online at https://doi.org/10.1016/j.micromeso.2025.114006.

Data availability

Data will be made available on request.

References

[1] F. Jamil, M. Aslam, A.H. Al-Muhtaseb, A. Bokhari, S. Rafiq, Z. Khan, A. Inayat, A. Ahmed, S. Hossain, M.S. Khurram, M.S. Abu Bakar, Greener and sustainable production of bioethylene from bioethanol: current status, opportunities and perspectives, Rev. Chem. Eng. 38 (2022) 185–207, https://doi.org/10.1515/revce-2019-0026.

[2] C.M. Mendieta, R.E. Cardozo, F.E. Felissia, N.M. Clauser, M.E. Vallejos, M.C. Area, Bioconversion of wood waste to bio-ethylene: a review, BioRes 16 (2021) 4411–4437, https://doi.org/10.15376/biores.16.2.Mendieta.

[3] V. Hulea, Toward platform chemicals from bio-based ethylene: heterogeneous catalysts and processes, ACS Catal. 8 (2018) 3263–3279, https://doi.org/10.1021/acscatal.7b04294.

[4] A. Mohsenzadeh, A. Zamani, M.J. Taherzadeh, Bioethylene production from ethanol: a review and techno-economical evaluation, ChemBioEng Rev. 4 (2017) 75–91, https://doi.org/10.1002/cben.201600025.

[5] H. Xiang, R. Xin, N. Prasongthum, P. Natewong, T. Sooknoi, J. Wang, P. Reubroycharoen, X. Fan, Catalytic conversion of bioethanol to value-added chemicals and fuels: a review, Resour. Chem. Mater. 1 (2022) 47–68, https://doi.org/10.1016/j.recm.2021.12.002.

[6] T.K. Phung, L. Proietti Hernández, A. Lagazzo, G. Busca, Dehydration of ethanol over zeolites, silica alumina and alumina: lewis acidity, brønsted acidity and confinement effects, Appl. Catal. Gen. 493 (2015) 77–89, https://doi.org/10.1016/j.apcata.2014.12.047.

[7] Z. Wang, L.A. O'Dell, X. Zeng, C. Liu, S. Zhao, W. Zhang, M. Gaborieau, Y. Jiang, J. Huang, Insight into three-coordinate aluminum species on ethanol-to-olefin conversion over ZSM-5 zeolites, Angew. Chem. Int. Ed. 58 (2019) 18061–18068, https://doi.org/10.1002/anie.201910987.

[8] G. Chen, S. Li, F. Jiao, Q. Yuan, Catalytic dehydration of bioethanol to ethylene over TiO2/γ-Al2O3 catalysts in microchannel reactors, Catal. Today 125 (2007) 111–119, https://doi.org/10.1016/j.cattod.2007.01.071.

[9] J. Bedia, R. Barrionuevo, J. Rodríguez-Mirasol, T. Cordero, Ethanol dehydration to ethylene on acid carbon catalysts, Appl. Catal. B Environ. 103 (2011) 302–310, https://doi.org/10.1016/j.apcatb.2011.01.032.

[10] Soo Ling Chong, Chee Soh Jiah, Chin Kui Cheng, Catalytic performance of H3PO4-modified cerium oxide as catalyst for ethylene production from ethanol dehydration, in: 5th International Conference on Advances in Chemical, Biological & Environmental Engineering (ACBEE-17), EAP, 2017, pp. 193–198, https://doi.org/10.17758/EAP.U0317207.
[11] A. Popa, V. Sasca, Catalytic conversion of ethanol over nickel salts of keggin type heteropolyacids supported on mesoporous silica, React. Kinet. Mech. Catal. 121 (2017) 657–672, https://doi.org/10.1007/s11144-017-1189-8.
[12] A.E.-A.A. Said, M.M.M. Abd El-Wahab, M.M. Abdelhak, The role of brønsted acid site strength on the catalytic performance of phosphotungstic acid supported on nano γ-alumina catalysts for the dehydration of ethanol to diethyl ether, React. Kinet. Mech. Catal. 122 (2017) 433–449, https://doi.org/10.1007/s11144-017-1207-x.
[13] R. Feng, X. Hu, X. Yan, Z. Yan, M.J. Rood, A high surface area mesoporous γ-Al2O3 with tailoring texture by glucose template for ethanol dehydration to ethylene, Microporous Mesoporous Mater. 241 (2017) 89–97, https://doi.org/10.1016/j.micromeso.2016.11.035.
[14] N. Ohtake, Y. Yamane, K. Nakagawa, M. Katoh, S. Sugiyama, Hydrothermally synthesized ceria with a high specific surface area for catalytic conversion of ethanol to ethylene, J. Chem. Eng. Jpn./JCEJ 49 (2016) 197–203, https://doi.org/10.1252/jcej.15we125.
[15] A. Styskalik, I. Kordoghli, C. Poleunis, A. Delcorte, Z. Moravec, L. Simonikova, V. Kanicky, C. Aprile, L. Fusaro, D.P. Debecker, Hybrid mesoporous aluminosilicate catalysts obtained by non-hydrolytic sol–gel for ethanol dehydration, J. Mater. Chem. A 8 (2020) 23526–23542, https://doi.org/10.1039/D0TA07016E.
[16] A. Styskalik, V. Vykoukal, L. Fusaro, C. Aprile, D.P. Debecker, Mildly acidic aluminosilicate catalysts for stable performance in ethanol dehydration, Appl. Catal. B Environ. 271 (2020) 118926, https://doi.org/10.1016/j.apcatb.2020.118926.
[17] D. Varisli, T. Dogu, G. Dogu, Petrochemicals from ethanol over a W–Si-based nanocomposite bidisperse solid acid catalyst, Chem. Eng. Sci. 65 (2010) 153–159, https://doi.org/10.1016/j.ces.2009.01.066.
[18] H. Wang, J. Ye, Y. Liu, Y. Li, Y. Qin, Steam reforming of ethanol over Co3O4/CeO2 catalysts prepared by different methods, Catal. Today 129 (2007) 305–312, https://doi.org/10.1016/j.cattod.2006.10.012.
[19] A. Salcedo, E. Poggio-Fraccari, F. Mariño, B. Irigoyen, Tuning the selectivity of cerium oxide for ethanol dehydration to ethylene, Appl. Surf. Sci. 599 (2022) 153963, https://doi.org/10.1016/j.apsusc.2022.153963.
[20] Q. Sheng, K. Ling, Z. Li, L. Zhao, Effect of steam treatment on catalytic performance of HZSM-5 catalyst for ethanol dehydration to ethylene, Fuel Process. Technol. 110 (2013) 73–78, https://doi.org/10.1016/j.fuproc.2012.11.004.
[21] D. Masih, S. Rohani, J.N. Kondo, T. Tatsumi, Catalytic dehydration of ethanol-to-ethylene over Rho zeolite under mild reaction conditions, Microporous Mesoporous Mater. 282 (2019) 91–99, https://doi.org/10.1016/j.micromeso.2019.01.035.
[22] C.-Y. Wu, H.-S. Wu, Ethylene formation from ethanol dehydration using ZSM-5 catalyst, ACS Omega 2 (2017) 4287–4296, https://doi.org/10.1021/acsomega.7b00680.
[23] J. Ouyang, F. Kong, G. Su, Y. Hu, Q. Song, Catalytic conversion of bio-ethanol to ethylene over La-Modified HZSM-5 catalysts in a bioreactor, Catal. Lett. 132 (2009) 64–74, https://doi.org/10.1007/s10562-009-0047-3.
[24] L. Wu, T. Zhou, Q. Cui, H. Wang, Y. Hu, H. Huang, The catalytic dehydration of bio-ethanol to ethylene on SAPO-34 catalysts, Petrol. Sci. Technol. 31 (2013) 2414–2421, https://doi.org/10.1080/10916466.2011.572102.
[25] A.G. Gayubo, A. Alonso, B. Valle, AndrésT. Aguayo, J. Bilbao, Selective production of olefins from bioethanol on HZSM-5 zeolite catalysts treated with NaOH, Appl. Catal. B Environ. 97 (2010) 299–306, https://doi.org/10.1016/j.apcatb.2010.04.021.
[26] L. Ouayloul, I. Agirrezabal-Telleria, P.L. Arias, F. Dumeignil, M.E. Doukkali, Tuning the acid nature of the ZSM-5 surface for selective production of ethylene from ethanol at low temperatures, Energy Fuels 38 (2024) 4492–4503, https://doi.org/10.1021/acs.energyfuels.3c04622.
[27] P.H. Finger, T.A. Osmari, N.M. Cabral, J.M.C. Bueno, J.M.R. Gallo, Direct synthesis of Cu supported on mesoporous silica: tailoring the Cu loading and the activity for ethanol dehydrogenation, Catal. Today 381 (2021) 26–33, https://doi.org/10.1016/j.cattod.2020.10.019.
[28] L.P. Rivoira, V.A. Valles, M.L. Martínez, Y. Sa-ngasaeng, S. Jongpatiwut, A. R. Beltramone, Catalytic oxidation of sulfur compounds over Ce-SBA-15 and Ce-Zr-SBA-15, Catal. Today 360 (2021) 116–128, https://doi.org/10.1016/j.cattod.2019.08.005.
[29] M. Shakeri, Z. Khatami Shal, P. Van Der Voort, An overview of the challenges and progress of synthesis, characterization and applications of plugged SBA-15 materials for heterogeneous catalysis, Materials 14 (2021) 5082, https://doi.org/10.3390/ma14175082.
[30] C.M. Aiube, K.V. de Oliveira, J.L. de Macedo, Effect of cerium precursor in the synthesis of Ce-MCM-41 and in the efficiency for liquid-phase oxidation of benzyl alcohol, Catalysts 9 (2019) 377, https://doi.org/10.3390/catal9040377.
[31] Y.W. Cheng, C.C. Chong, C.K. Cheng, K.H. Ng, T. Witoon, J.C. Juan, Ethylene production from ethanol dehydration over mesoporous SBA-15 catalyst derived from palm oil clinker waste, J. Clean. Prod. 249 (2020) 119323, https://doi.org/10.1016/j.jclepro.2019.119323.
[32] P. Kaminski, The application of FTIR in situ spectroscopy combined with methanol adsorption to the study of mesoporous sieve SBA-15 with cerium-zirconium oxides modified with gold and copper species, Arab. J. Chem. 13 (2020) 851–862, https://doi.org/10.1016/j.arabjc.2017.08.004.
[33] J. Yang, Y. Jia, B. Huang, X. Li, L. Guo, A. Zheng, R. Luque, Y. Sun, Functionalized CeO_2/SBA-15 materials as efficient catalysts for aqueous room temperature mono-dehydration of sugar alcohols, ACS Sustainable Chem. Eng. 8 (2020) 6371–6380, https://doi.org/10.1021/acssuschemeng.0c00494.
[34] S. Saravanamurugan, A. Riisager, Solid acid catalysed formation of ethyl levulinate and ethyl glucopyranoside from mono- and disaccharides, Catal. Commun. 17 (2012) 71–75, https://doi.org/10.1016/j.catcom.2011.10.001.
[35] V. Hegde, P. Pandit, P. Rananaware, V.P. Brahmkhatri, Sulfonic acid-functionalized mesoporous silica catalyst with different morphology for biodiesel production, Front. Chem. Sci. Eng. 16 (2022) 1198–1210, https://doi.org/10.1007/s11705-021-2133-z.
[36] Functionalized Mesoporous SBA-15 Silica: Recent Trends and Catalytic Applications - Nanoscale (RSC Publishing) DOI:10.1039/D0NR00732C, (n.d.). https://pubs.rsc.org/en/content/articlehtml/2023/ey/d0nr00732c (accessed September 2, 2025).
[37] C. Autthanit, P. Praserthdam, B. Jongsomjit, Oxidative and non-oxidative dehydrogenation of ethanol to acetaldehyde over different VOx/SBA-15 catalysts, J. Environ. Chem. Eng. 6 (2018) 6516–6529, https://doi.org/10.1016/j.jece.2018.10.015.
[38] T.K. Phung, G. Busca, Diethyl ether cracking and ethanol dehydration: acid catalysis and reaction paths, Chem. Eng. J. 272 (2015) 92–101, https://doi.org/10.1016/j.cej.2015.03.008.
[39] R.G. Herman, F.H. Khouri, K. Klier, J.B. Higgins, M.R. Galler, C.R. Terenna, Dehydrocondensation of alcohols to form ethers over mesoporous SBA-15 catalyst, J. Catal. 228 (2004) 347–361, https://doi.org/10.1016/j.jcat.2004.09.012.
[40] X. Yu, C.T. Williams, Recent advances in the applications of mesoporous silica in heterogeneous catalysis, Catal. Sci. Technol. 12 (2022) 5765–5794, https://doi.org/10.1039/D2CY00001F.
[41] M.L. Testa, V. La Parola, Sulfonic acid-functionalized inorganic materials as efficient catalysts in various applications: a minireview, Catalysts 11 (2021) 1143, https://doi.org/10.3390/catal11101143.
[42] N.G. Kobylinska, O.A. Dudarko, I.V. Melnyk, G.A. Seisenbaeva, V.G. Kessler, Luminescence performance of Cerium(III) ions incorporated into organofunctional mesoporous silica, Microporous Mesoporous Mater. 305 (2020) 110331, https://doi.org/10.1016/j.micromeso.2020.110331.
[43] V.N. Zaitsev, N.G. Kobylinskaya, L.S. Kostenko, V.I. Gerda, Conductometric determination of the concentration of acid centers on functionalized materials, J. Anal. Chem. 63 (2008) 779–786, https://doi.org/10.1134/S1061934808080121.
[44] J. Tauc, R. Grigorovici, A. Vancu, Optical properties and electronic structure of amorphous germanium, Phys. Status Solidi 15 (1966) 627–637, https://doi.org/10.1002/pssb.19660150224.
[45] M. Thommes, K. Kaneko, A.V. Neimark, J.P. Olivier, F. Rodriguez-Reinoso, J. Rouquerol, K.S.W. Sing, Physisorption of gases, with special reference to the evaluation of surface area and pore size distribution (IUPAC Technical Report), Pure Appl. Chem. 87 (2015) 1051–1069, https://doi.org/10.1515/pac-2014-1117.
[46] G. Gran, Determination of the equivalence point in potentiometric titrations. Part II, Analyst 77 (1952) 661–671, https://doi.org/10.1039/AN9527700661.
[47] S. Molaei, T. Tamoradi, M. Ghadermazi, A. Ghorbani-Choghamarani, Ordered mesoporous SBA-15 functionalized with yttrium(III) and cerium(III) complexes: towards active heterogeneous catalysts for oxidation of sulfides and preparation of 5-substituted 1 *H* -tetrazoles, Appl. Organomet. Chem. 33 (2019) e4649, https://doi.org/10.1002/aoc.4649.
[48] R. Rashid, F. Afroze, S. Ahmed, M. Shah Miran, A. Bin, H. Susan, Control of the porosity and morphology of ordered mesoporous silica by varying calcination conditions, Mater. Today Proc. 15 (2019) 546–554, https://doi.org/10.1016/j.matpr.2019.04.119.
[49] A.S. Thill, F.O. Lobato, M.O. Vaz, W.P. Fernandes, V.E. Carvalho, E.A. Soares, F. Poletto, S.R. Teixeira, F. Bernardi, Shifting the band gap from UV to visible region in cerium oxide nanoparticles, Appl. Surf. Sci. 528 (2020) 146860, https://doi.org/10.1016/j.apsusc.2020.146860.
[50] D.J. Morgan, Photoelectron spectroscopy of ceria: reduction, quantification and the myth of the vacancy peak in XPS analysis, Surf. Interface Anal. 55 (2023) 845–850, https://doi.org/10.1002/sia.7254.
[51] P. Yu, S.A. Hayes, T.J. O'Keefe, M.J. O'Keefe, J.O. Stoffer, The phase stability of cerium species in aqueous systems, J. Electrochem. Soc. 153 (2006) C74, https://doi.org/10.1149/1.2130572.
[52] A. Bensalem, J.C. Muller, F. Bozon-Verduraz, Faraday communications. From bulk CeO_2 to supported cerium–oxygen clusters: a diffuse reflectance approach, J. Chem. Soc., Faraday Trans. 88 (1992) 153–154, https://doi.org/10.1039/FT9928800153.